mathematics

MDPI

Article

A 2.5D Generalized Finite Difference Method for Elastic Wave Propagation Problems

Hao Chang [1], Fajie Wang [1,*], Xingxing Yue [2], Lin Qiu [1] and Linlin Sun [3,*]

[1] College of Mechanical and Electrical Engineering, Qingdao University, Qingdao 266071, China; ch25dh@163.com (H.C.); linqiu@qdu.edu.cn (L.Q.)
[2] College of Materials Science and Engineering, Qingdao University, Qingdao 266071, China; qdxxy90@qdu.edu.cn
[3] School of Science, Nantong University, Nantong 226019, China
* Correspondence: wfj1218@126.com (F.W.); rudong9110@163.com (L.S.)

Abstract: The analysis of elastic wave propagation is a critical problem in both science and engineering, with applications in structural health monitoring and seismic wave analysis. However, the efficient and accurate numerical simulation of large-scale three-dimensional structures has posed significant challenges to traditional methods, which often struggle with high computational costs and limitations. This paper presents a novel two-and-a-half-dimensional generalized finite difference method (2.5D GFDM) for efficient simulation of elastic wave propagation in longitudinally invariant structures. The proposed scheme integrates GFDM with 2.5D technology, reducing 3D problems to a series of 2D problems in the wavenumber domain via Fourier transforms. Subsequently, the solutions to the original 3D problems can be recovered by performing inverse Fourier transforms on the solutions obtained from the 2D problems. The 2.5D GFDM avoids the inherent challenge of mesh generation in traditional methods like FEM and FVM, offering a meshless solution for complex 3D problems. By employing sparse coefficient matrices, it offers significantly improved computational efficiency. The new approach achieves significant computational advantages while maintaining high accuracy, as validated through three representative examples, making it a promising tool for solving large-scale elastic wave propagation problems in longitudinally invariant structures.

Keywords: elastic wave propagation; meshless method; generalized finite difference method; 2.5D techniques; longitudinally invariant structures

MSC: 35Q74; 74H15; 42A38

check for updates

Academic Editor: Carlo Bianca

Received: 14 March 2025
Revised: 6 April 2025
Accepted: 8 April 2025
Published: 10 April 2025

Citation: Chang, H.; Wang, F.; Yue, X.; Qiu, L.; Sun, L. A 2.5D Generalized Finite Difference Method for Elastic Wave Propagation Problems. *Mathematics* **2025**, *13*, 1249. https://doi.org/10.3390/math13081249

Copyright: © 2025 by the authors. Licensee MDPI, Basel, Switzerland. This article is an open access article distributed under the terms and conditions of the Creative Commons Attribution (CC BY) license (https://creativecommons.org/licenses/by/4.0/).

1. Introduction

Numerical simulation of elastic wave propagation is a critical tool in various fields of science and engineering [1–5], with applications ranging from designing earthquake-resistant structures and ultrasonic testing to analyzing ground vibrations caused by subway operations. Commonly used numerical methods for addressing these challenges include the finite element method (FEM) [6–9], the finite difference method (FDM) [10,11], and the boundary element method (BEM) [12–15]. However, traditional mesh-based numerical methods face significant challenges when dealing with such problems. Specifically, to achieve reliable computational results, at least six degrees of freedom (DOFs) per wavelength are typically required along each coordinate axis. As the ratio of wavelength/frequency and the characteristic length increases, the computational cost of these

mesh-based methods rises quadratically, leading to a rapid escalation in computational burden for high-frequency or large-scale problems. To address these limitations, researchers have developed more advanced techniques, such as plane-wave BEM [16], spectral FDM/FEM [17], wave-based FEM [18], and hybrid Trefftz FEM [19–21], to simulate elastic wave propagation more efficiently. Despite these advancements, these methods still depend on mesh discretization, and the quality of the mesh remains a critical factor influencing their computational accuracy and efficiency.

In order to simplify computations and enhance efficiency, numerous meshless/meshfree methods have been developed over the past two decades. These include the singular boundary method [22–25], the fundamental solution method [26,27], the LRBFCM [28], the boundary particle method [29], the Trefftz method [30,31], the radial integration method [32], the boundary knot method [33], the Spatio-temporal meshless method [34], the particular solution method [35,36], and the generalized finite difference method (GFDM) [37–47], among others. Meshless methods eliminate the need for mesh generation and numerical integration, significantly reducing computational time and resource requirements. Among these approaches, the GFDM stands out as one of the most promising domain-type mesh-free methods due to its robust performance and potential applications. The GFDM is an evolution of the classical finite difference method, built upon Taylor series expansion and the moving least squares method. This approach eliminates the dependency on meshes and does not require numerical integration. Its fundamental concept involves approximating the derivatives of unknown variables as a linear combination of values at neighboring nodes within a star. Moreover, the coefficient matrix generated by the GFDM is typically sparse, offering significant computational efficiency compared to the dense matrices produced by boundary-type meshless methods. In 1998, Orkisz [48] laid the theoretical foundation for the GFDM, introducing key techniques such as node generation, local approximation, and node star. Later, in 2001, Benito et al. [37] further advanced the GFDM by developing its explicit formulation and systematically investigating various factors affecting its computational accuracy [38]. As the theory behind the GFDM has gradually been refined, researchers have begun applying it to practical engineering problems. The GFDM has been successfully used to solve a range of complex issues, including the nonlinear heat conduction equation [43], the two-dimensional nonlinear obstacle problem [41], the three-dimensional inhomogeneous Helmholtz-type equation [45], thermoelastic wave propagation analysis [44], double-diffusive natural convection in fluid-saturated porous media [49], the stationary 2D and 3D Stokes equations with a mixed boundary condition [50], the surface PDEs [51], the bending equation of Reissner elastic plates [52], the nonlinear elliptic partial differential equations [43], and the long-term dynamic modeling of 3D coupled thermoelastic problems [53], among others. These studies demonstrate that the GFDM not only provides excellent computational efficiency when handling complex partial differential equations but also accurately addresses various practical engineering challenges, showcasing its broad applicability and significant potential for engineering applications.

For columnar three-dimensional structures of infinite longitudinal extent, where the geometry and material properties are approximately invariant along the longitudinal cross-section, directly applying the meshless methods in their three-dimensional (3D) form results in prohibitively high computational costs. This is even more challenging for mesh-based methods when applied to such problems. As a result, a so-called two-and-a-half-dimensional (2.5D) model has been proposed as a substitute for full 3D analysis. The 2.5D method demonstrates significant advantages in the computation of such columnar three-dimensional structures. The method begins by applying a spatial Fourier transform along the direction with invariant geometry, thereby converting the problem into the

wavenumber domain. This transformation reduces the original 3D problem to a series of 2D problems, each corresponding to a specific wavenumber. Once the 2D problems are solved for their respective wavenumbers, the solutions to the 3D problem can be obtained by performing an inverse spatial Fourier transform on the 2D solutions. Numerous studies have integrated 2.5D methods with traditional approaches such as the finite element method (FEM). For instance, Ma et al. [54] proposed a 2.5D FEM-PML method for longitudinally bending viscoelastic structures, which relies on the perfectly matched layer (PML) to simulate infinite domains. In recent years, meshless methods, represented by the method of fundamental solutions (MFS) and the singular boundary method (SBM), have achieved significant breakthroughs by eliminating mesh dependency. The SBM, in particular, places source points directly on physical boundaries and introduces origin intensity factors (OIFs) to regularize singularities. For instance, in 2020, Sun et al. [55] applied the SBM to simulate elastic wave propagation in two-dimensional partially saturated poroelastic media. Later in 2022, Wei et al. [56] first extended the SBM to dynamic response analysis of saturated half-space soils for ground vibration prediction. Additionally, Gu et al. [57] pioneered the application of the SBM to orthotropic elastic problems. To address multiphysics and large-scale problems, hybrid strategies combining 2.5D methods with FEM, BEM, and meshless methods have gained traction. Liravi et al. [58] improved the efficiency of soil-structure interaction analysis by using FEM for structural modeling and SBM for soil media in 2022; later, in 2024, they combined the SBMs robustness for sharp boundaries with the MFSs accuracy for smooth boundaries, validating their approach in a cavity problem with a five-cusped hypocycloid cross-section [59]. Sun et al. [60] achieved efficient 3D elastic wave simulation by employing a localized collocation solver to sparsify dense matrices and reduce computational costs. Aubry et al. [61] utilized a 2.5D approach to study the response of an infinite beam and an elastic half-space under moving loads. Sheng et al. [62,63] applied this method to model infinite-layer beams coupled with a layered half-space for railway track systems. Zeng et al. [64] proposed a novel resistivity logging simulation scheme for anisotropic media based on the 2.5D finite difference method. Suchde [65] proposes a novel model-adaptive framework that dynamically couples 3D incompressible Navier-Stokes equations with a pseudo-2D thin film flow model (Discrete Droplet Method) to efficiently simulate complex free-surface flows involving both bulk and thin-film regimes. Yang et al. [66] proposed a generalized 2.5D time-domain seismic wave equation, compatible with acoustic, elastic isotropic/anisotropic media and complex topographic boundaries. Additionally, Amado-Mendes et al. [67] employed a 2.5D MFS-FEM model to analyze ground and tunnel vibrations induced by railway traffic. The above studies demonstrate that 2.5D methods significantly reduce both the time required to construct models and the computational costs needed. Compared to traditional 3D methods for addressing such problems, the 2.5D approach offers substantial advantages. In this context, considering the respective advantages of the meshless GFDM and 2.5D techniques, this paper combines the 2.5D technique with the GFDM, proposing a more advanced meshless method, namely, the 2.5D generalized finite difference method (2.5D GFDM).

This manuscript is structured as follows: the initial section outlines the relevant literature review and the objectives of this study. Section 2 details the streamlined derivation of the governing equations. Subsequently, Section 3 delineates the novel 2.5D meshless numerical approaches. Section 4 presents three numerical examples to assess the efficacy of the proposed methodology. Finally, Section 5 offers some discussions of the findings and conclusions drawn from the numerical outcomes and comparative analyses.

2. Elastic Wave Propagation Problems

For a homogeneous isotropic linear elastic medium, the source-free 3D wave equation is given by

$$\begin{cases} \rho\partial_{tt}U_x = \partial_x\sigma_{xx} + \partial_y\sigma_{xy} + \partial_z\sigma_{zx} \\ \rho\partial_{tt}U_y = \partial_x\sigma_{xy} + \partial_y\sigma_{yy} + \partial_z\sigma_{zy} \\ \rho\partial_{tt}U_z = \partial_x\sigma_{xz} + \partial_y\sigma_{zy} + \partial_z\sigma_{zz} \end{cases}, \tag{1}$$

where ρ is the mass density, $\left[U_x, U_y, U_z\right] = \mathbf{U}(x, y, z, t)$ stands for the displacements at a point $\mathbf{x} = (x, y, z)$ at time t, $\sigma_{ij} = \boldsymbol{\sigma}(x, y, z, t)$, $(i, j = x, y, z)$ are stress components. A contracted notation is adopted for representing derivatives: $\partial_{tt} = \partial^2/\partial t^2$, and $\partial_r = \partial/\partial r$, $(r = x, y, z)$. The stress and displacement components are related by the 3D Hooke's law through the Lamé constants λ and μ as follows:

$$\begin{cases} \sigma_{xx} = (\lambda + 2\mu)\partial_x U_x + \lambda\left(\partial_y U_y + \partial_z U_z\right) \\ \sigma_{yy} = (\lambda + 2\mu)\partial_y U_y + \lambda(\partial_z U_z + \partial_x U_x) \\ \sigma_{zz} = (\lambda + 2\mu)\partial_z U_z + \lambda\left(\partial_x U_x + \partial_y U_y\right) \\ \sigma_{yz} = \sigma_{zy} = \mu\left(\partial_z U_y + \partial_y U_z\right) \\ \sigma_{xz} = \sigma_{zx} = \mu(\partial_x U_z + \partial_z U_x) \\ \sigma_{xy} = \sigma_{yx} = \mu\left(\partial_y U_x + \partial_x U_y\right) \end{cases}, \tag{2}$$

where the Lamé constants λ and μ are defined as

$$\lambda = \frac{\nu E}{(1+\nu)(1-2\nu)}, \mu = \frac{E}{2(1+\nu)}, \tag{3}$$

in which E and ν are the modulus of elasticity and Poisson's ratio, respectively.

By performing a Fourier transform of Equation (1) with respect to t, we obtain the following source-free 3D elastodynamic equation in the frequency domain:

$$\begin{cases} -\omega^2\rho u_x = \partial_x\hat{\sigma}_{xx} + \partial_y\hat{\sigma}_{xy} + \partial_z\hat{\sigma}_{zx} \\ -\omega^2\rho u_y = \partial_x\hat{\sigma}_{xy} + \partial_y\hat{\sigma}_{yy} + \partial_z\hat{\sigma}_{zy} \\ -\omega^2\rho u_z = \partial_x\hat{\sigma}_{xz} + \partial_y\hat{\sigma}_{zy} + \partial_z\hat{\sigma}_{zz} \end{cases}, \tag{4}$$

where $\left[u_x, u_y, u_z\right] = \mathbf{u}(x, y, z, \omega)$ and $\hat{\sigma}_{ij}(i, j = x, y, z)$ denote the Fourier transforms of $\left[U_x, U_y, U_z\right]$ and $\sigma_{ij}(i, j = x, y, z)$, respectively. By substituting Equation (3) into Equation (2), the frequency-domain elastic wave equation for linear isotropic homogeneous media with a 3D domain Ω, enclosed by the boundary Γ, is derived as,

$$\alpha^2(\nabla\nabla\cdot\mathbf{u}) - \beta^2\nabla\times\nabla\times\mathbf{u} + \omega^2\mathbf{u} = 0,\ \mathbf{x}\in\Omega, \tag{5}$$

where $\alpha = \sqrt{(\lambda+2\mu)/\rho}$ denotes the P wave velocity, $\beta = \sqrt{\mu/\rho}$ the S wave velocity, $\nabla = \left[\frac{\partial}{\partial x}, \frac{\partial}{\partial y}, \frac{\partial}{\partial z}\right]$ the gradient operator, $\omega = 2\pi f$ the angular frequency, with f being the frequency in Hertz. For this boundary value problem, Dirichlet or Neumann boundary conditions are typically imposed, as follows:

$$\mathbf{u} = \mathbf{u}_b,\ x\in\Gamma, \tag{6}$$

$$\mathrm{t} = \hat{\boldsymbol{\sigma}}\cdot\mathbf{n} = \mathbf{t}_b, \mathbf{x}\in\Gamma, \tag{7}$$

where $\mathbf{n} = \left[n_x, n_y, n_z\right]$ denotes the outward normal unit vector at the boundary, three traction field components and nine stress components are represented by vectors $\mathbf{t}$ and $\hat{\boldsymbol{\sigma}}$. The boundary conditions are defined by the prescribed displacement and traction values, which are denoted by vectors $\mathbf{u}_b$ and $\mathbf{t}_b$, respectively.

3. 2.5D GFDM for Elastic Wave Propagation Problems

Consider the model to be infinitely extended along the z-direction, with its mechanical and geometrical parameters invariant in this direction; that is, the material and geometry do not change along the z-axis. Therefore, it is convenient to solve the problem in the frequency-wavenumber domain, known as the 2.5D method. The problems described above are the type that the 2.5D method proposed in this paper aims to address. With z as the invariant direction, the governing equation and boundary conditions can be transformed to the frequency-wavenumber domain by applying the spatial Fourier transform to Equations (5)–(7) along the z-direction, as follows:

$$\alpha^2\left(\widetilde{\nabla}\widetilde{\nabla}\cdot\widetilde{\mathbf{u}}\right)-\beta^2\widetilde{\nabla}\times\widetilde{\nabla}\times\widetilde{\mathbf{u}}+\omega^2\widetilde{\mathbf{u}}=0, \tag{8}$$

$$\widetilde{\mathbf{u}}=\widetilde{\mathbf{u}}_b,\widetilde{\mathbf{x}}\in\widetilde{\Gamma}, \tag{9}$$

$$\widetilde{\mathbf{t}}=\widetilde{\boldsymbol{\sigma}}\cdot\mathbf{n}=\widetilde{\mathbf{t}}_b\widetilde{\mathbf{x}}\in\widetilde{\Gamma}, \tag{10}$$

where $\widetilde{\nabla}=\left[\frac{\partial}{\partial x},\frac{\partial}{\partial y},\mathrm{i}k_z\right]$ is the Fourier transform of the gradient operator $\nabla=\left[\frac{\partial}{\partial x},\frac{\partial}{\partial y},\frac{\partial}{\partial z}\right]$,

$$\widetilde{\mathbf{t}}(x,y,k_z)=\int_{-\infty}^{+\infty}\mathbf{t}(x,y,z)e^{-\mathrm{i}k_zz}dz, \tag{11}$$

$$\widetilde{\mathbf{u}}(x,y,k_z)=\int_{-\infty}^{+\infty}\mathbf{u}(x,y,z)e^{-ik_zz}dz, \tag{12}$$

in which

$$\mathbf{u}(x,y,z)=\frac{1}{2\pi}\int_{-\infty}^{+\infty}\widetilde{\mathbf{u}}(x,y,k_z)e^{\mathrm{i}k_zz}dk_z. \tag{13}$$

It can be observed that the derivatives related to z are replaced by k_z which represents the spatial wavenumber associated with the longitudinal z-direction, i denotes the imaginary unit. The derivation detailed in [68] provides a comprehensive development of the described procedure; for the sake of conciseness, it is omitted from the present manuscript.

The integral resembling the inverse Fourier transform is computed using numerical methods. However, the approximate solution $\widetilde{\mathbf{u}}$ exhibits singular behavior at $|k_z|=k_p$ or $|k_z|=k_s$. To circumvent the issue of singular values during the integration and to enhance the precision of the computation, a novel formulation for Equation (13) has been developed, which is as follows:

$$\mathbf{u}(x,y,z)=\mathbf{u}_1(x,y,z)+\mathbf{u}_2(x,y,z)+\mathbf{u}_3(x,y,z)+\mathbf{u}_4(x,y,z)+\mathbf{u}_5(x,y,z), \tag{14}$$

in which

$$\begin{aligned}\mathbf{u}_1(x,y,z)=&\frac{1}{2\pi}\int_{-\infty}^{-\beta_2k_s}\widetilde{\mathbf{u}}(x,y,k_z)e^{\mathrm{i}k_zz}dk_z\\&+\frac{1}{2\pi}\int_0^{-k_s\sqrt{\beta_2^2-1}}\widetilde{\mathbf{u}}(x,y,w_{sl})e^{\mathrm{i}\sqrt{k_s^2+w_{sl}^2}z}\frac{w_{sl}}{\sqrt{k_s^2-w_{sl}^2}}dw_{sl},\end{aligned} \tag{15}$$

$$\begin{aligned}\mathbf{u}_2(x,y,z)=&\frac{1}{2\pi}\int_0^{-k_s\sqrt{1-\beta_1^2}}\widetilde{\mathbf{u}}(x,y,v_{sl})e^{\mathrm{i}\sqrt{k_s^2-v_{sl}^2}z}\frac{v_{sl}}{\sqrt{k_s^2-v_{sl}^2}}dv_{sl}\\&+\frac{1}{2\pi}\int_{-\beta_1k_s}^{-\beta_2k_p}\widetilde{\mathbf{u}}(x,y,k_z)e^{\mathrm{i}k_zz}dk_z\\&+\frac{1}{2\pi}\int_0^{-k_p\sqrt{\beta_2^2-1}}\widetilde{\mathbf{u}}(x,y,w_{pr})e^{\mathrm{i}\sqrt{k_p^2+w_{pr}^2}z}\frac{w_{pr}}{\sqrt{k_p^2+w_{pr}^2}}dw_{pr},\end{aligned} \tag{16}$$

$$\begin{aligned}\mathbf{u}_3(x,y,z) = &\frac{1}{2\pi}\int_0^{-k_p\sqrt{1-\beta_1^2}} \widetilde{\mathbf{u}}\Big(x,y,v_{pl}\Big)e^{-\mathrm{i}\sqrt{k_p^2-v_{pl}^2}z}\frac{v_{pl}}{\sqrt{k_p^2-v_{pl}^2}}dv_{pl}\\ &+\frac{1}{2\pi}\int_{-\beta_1 k_p}^{\beta_1 k_p} \widetilde{\mathbf{u}}(x,y,k_z)e^{\mathrm{i}k_z z}dk_z\\ &+\frac{1}{2\pi}\int_0^{k_p\sqrt{1-\beta_1^2}} \widetilde{\mathbf{u}}(x,y,v_{pr})e^{\mathrm{i}\sqrt{k_p^2-v_{pr}^2}z}\frac{v_{pr}}{\sqrt{k_p^2-v_{pr}^2}}dv_{pr},\end{aligned} \tag{17}$$

$$\begin{aligned}\mathbf{u}_4(x,y,z) = &\frac{1}{2\pi}\int_0^{k_p\sqrt{\beta_2^2-1}} \widetilde{\mathbf{u}}\Big(x,y,w_{pl}\Big)e^{\mathrm{i}\sqrt{k_p^2+w_{pl}^2}z}\frac{w_{pl}}{\sqrt{k_p^2+w_{pl}^2}}dw_{pl}\\ &+\frac{1}{2\pi}\int_{\beta_2 k_p}^{\beta_1 k_s} \widetilde{\mathbf{u}}(x,y,k_z)e^{\mathrm{i}k_z z}dk_z\\ &+\frac{1}{2\pi}\int_{k_s}^{k_s\sqrt{1-\beta_1^2}} \widetilde{\mathbf{u}}(x,y,v_{sr})e^{\mathrm{i}\sqrt{k_s^2-v_{sr}^2}z}\frac{v_{sr}}{\sqrt{k_s^2-v_{sr}^2}}dv_{sr},\end{aligned} \tag{18}$$

$$\begin{aligned}\mathbf{u}_5(x,y,z) = &\frac{1}{2\pi}\int_{k_s}^{k_s\sqrt{\beta_2^2-1}} \widetilde{\mathbf{u}}(x,y,w_{sr})e^{\mathrm{i}\sqrt{k_s^2+w_{sr}^2}z}\frac{w_{sr}}{\sqrt{k_s^2+w_{sr}^2}}dw_{sr}\\ &+\frac{1}{2\pi}\int_{\beta_2 k_s}^{+\infty} \widetilde{\mathbf{u}}(x,y,k_z)e^{\mathrm{i}k_z z}dk_z,\end{aligned} \tag{19}$$

where $v_{pl} = -\sqrt{k_p^2-k_z^2}$, $v_{pr} = \sqrt{k_p^2-k_z^2}$, $v_{sl} = -\sqrt{k_s^2-k_z^2}$, $w_{pr} = -\sqrt{k_z^2-k_p^2}$, $w_{pl} = \sqrt{k_z^2-k_p^2}$, $v_{sr} = \sqrt{k_s^2-k_z^2}$, $w_{sl} = -\sqrt{k_z^2-k_s^2}$, $w_{sr} = \sqrt{k_z^2-k_s^2}$, $0 < \beta_1 < 1$ and $\beta_2 > 1$. In this paper, the values of β_1 and β_2 are taken as 0.95 and 1.05. The integration limits are truncated at $|k_z| = k_p$ and $|k_z| = k_s$, being divided into five intervals. Each interval is further divided into singular integration limits, which are near singular points, and non-singular integration limits, which are away from singular points. For the integrals that fall within the singular limits, a variable substitution as shown in Equations (15)–(19) is applied, which enables the integration to bypass the singular points. It is noteworthy that during the calculation of the Fourier transform, the Hankel function experiences rapid decay when $|k_z| > k_s$. Consequently, to minimize computational resources, we have chosen the integration limits for Equation (14) to be $[-\gamma k_s, \gamma k_s]$.

For computational convenience, Equation (8) can be expressed in the following form:

$$\begin{cases}(\lambda+2\mu)\frac{\partial^2\widetilde{u}_x}{\partial x^2}+\mu\frac{\partial^2\widetilde{u}_x}{\partial y^2}+\left(\omega^2\rho-\mu k_z^2\right)\widetilde{u}_x+(\lambda+\mu)\frac{\partial^2\widetilde{u}_y}{\partial x\partial y}+\mathrm{i}k_z(\lambda+\mu)\frac{\partial\widetilde{u}_z}{\partial x}=0\\ (\lambda+2\mu)\frac{\partial^2\widetilde{u}_y}{\partial y^2}+\mu\frac{\partial^2\widetilde{u}_y}{\partial x^2}+\left(\omega^2\rho-\mu k_z^2\right)\widetilde{u}_y+(\lambda+\mu)\frac{\partial^2\widetilde{u}_x}{\partial x\partial y}+\mathrm{i}k_z(\lambda+\mu)\frac{\partial\widetilde{u}_z}{\partial y}=0\\ \mathrm{i}k_z(\lambda+\mu)\frac{\partial\widetilde{u}_x}{\partial x}+\mathrm{i}k_z(\lambda+\mu)\frac{\partial\widetilde{u}_y}{\partial y}+\mu\frac{\partial^2\widetilde{u}_z}{\partial x^2}+\mu\frac{\partial^2\widetilde{u}_z}{\partial y^2}+\left[\omega^2\rho-k_z^2(\lambda+2\mu)\right]\widetilde{u}_z=0\end{cases}. \tag{20}$$

The above equation can be defined as a 2D equation of $\left[\widetilde{u}_x,\widetilde{u}_y,\widetilde{u}_z\right] = \widetilde{\mathbf{u}}(x,y,k_z)$. By applying Equation (13), we can compute the 3D displacement field $\mathbf{u}(x,y,z)$ in the frequency domain by solving $\widetilde{\mathbf{u}}(x,y,k_z)$ for every k_z.

The problem (5) will be solved by the 2.5D generalized finite difference method (2.5D GFDM), a meshless method developed from Taylor series expansion of multivariate functions and weighted moving least squares. The 2.5D approach enables the solution of 3D problems by utilizing a wavenumber-dependent 2D cross-sectional formulation. In this study, the z-direction is designated as the axis of geometrical invariance, allowing the reduction of the discretization domain from three dimensions to two. Within the 2.5D framework, the location of any given point is specified by a pair of values in a vector, which correspond to its Cartesian coordinates within the cross-sectional plane of the system. In contrast, displacements and tractions are represented by three-element vectors that capture their values along each of the three coordinate axes. Therefore, the mathematical procedures of the GFDM will be illustrated using the 2D case as an example.

In the GFDM, the derivative of an uncharted variable in the governing equation is estimated through a linear combination of the function values at its adjacent nodes. For numerical simulation, a set of N_b boundary nodes and N_i interior nodes are distributed uniformly or randomly along the boundary Γ and in the computational domain Ω, respectively. For a designated i^{th} node $X_c(x_c, y_c)$ named the central node, the m surrounding nodes $X_k(x_k, y_k)(k = 1, 2, \ldots, m)$ within proximity, along with the central node, are enclosed within a circular perimeter to create a supporting domain star, as depicted in Figure 1. A review of prior research [45,49] suggests that the stability and precision of numerical solutions are ensured when the m is greater than 10.

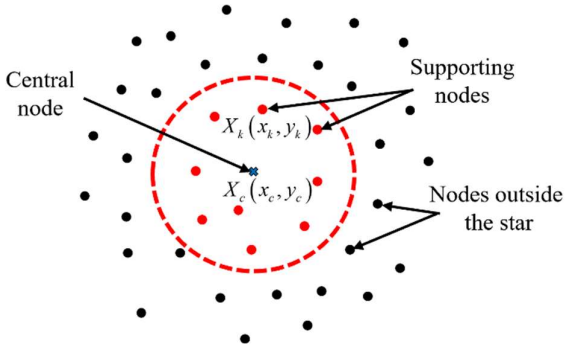


Figure 1. An irregular point cloud and the local GFDM star for a 2D case.

With the central node X_c designated and its corresponding star established, the Taylor series expansion for each node within the star can be utilized to expand the function, as described subsequently:

$$u_k = u_c + h_k \frac{\partial u_c}{\partial x} + l_k \frac{\partial u_c}{\partial y} + \frac{h_k^2}{2} \frac{\partial^2 u_c}{\partial x^2} + \frac{l_k^2}{2} \frac{\partial^2 u_c}{\partial y^2} + h_k l_k \frac{\partial^2 u_c}{\partial x \partial y} + \cdots, k = 1, 2, \ldots, m. \quad (21)$$

where h_k and l_k denote the distance between the supporting node $X_k(x_k, y_k)(k = 1, 2, \ldots, m)$ and the central node $X_c(x_c, y_c)$ in x- and y-directions:

$$h_k = x_k - x_c,\ k = 1, 2, \ldots, m. \quad (22)$$

$$l_k = y_k - y_c,\ k = 1, 2, \ldots, m. \quad (23)$$

$u_k = u(x_k, y_k)$ and $u_c = u(x_c, y_c)$ denote the function value at the nodes $X_k(x_k, y_k)$ $(k = 1, 2, \ldots, m)$ and $X_c(x_c, y_c)$, respectively. $\frac{\partial u_c}{\partial x}$, $\frac{\partial u_c}{\partial y}$, $\frac{\partial^2 u_c}{\partial x^2}$, $\frac{\partial^2 u_c}{\partial y^2}$, $\frac{\partial^2 u_c}{\partial x \partial y}$, are the derivatives at the node $X_c(x_c, y_c)$. By limiting the Taylor series expansions to include only up to the second-order derivatives, the residual function $B(u)$ is defined in the subsequent manner:

$$B(u) = \sum_{k=1}^{m} \left[\left(u_c - u_k + h_k \frac{\partial u_c}{\partial x} + l_k \frac{\partial u_c}{\partial x} + \frac{h_k^2}{2} \frac{\partial^2 u_c}{\partial x^2} + \frac{l_k^2}{2} \frac{\partial^2 u_c}{\partial y^2} + h_k l_k \frac{\partial^2 u_c}{\partial x \partial y} \right) w_k \right]^2, \quad (24)$$

in which w_k is the weighting coefficient at X_k and represents the importance of the approximations by Taylor series expansion at different nodes in the star of the node X_c. The weighting coefficient suggests that the Taylor series approximation at a node X_k is more influential if the node is in closer proximity to the central node X_c. With greater separation from a node X_c, the weight coefficient exhibits a corresponding reduction. A multitude of options for the weighting coefficient can be found in the extant literature [69], including

potential functions and cubic splines, among others. In this study, the weighting coefficient is adopted in the following form:

$$w_k = \begin{cases} 1 - 6\left(\frac{d_k}{d_m}\right)^2 + 8\left(\frac{d_k}{d_m}\right)^3 - 3\left(\frac{d_k}{d_m}\right)^4, & d_k \le d_m, \\ 0, & d_k > d_m, \end{cases} \tag{25}$$

in which $d_k = \sqrt{h_k^2 + l_k^2}$ denotes the distance between nodes X_k and X_c, and d_m represents the distance between the farthest node and the node X_c within the star. The partial derivatives at a node X_c appeared in Equation (24) are represented by

$$\boldsymbol{D}_u = \left[\left.\frac{\partial u_c}{\partial x}\right|_{X_c}, \left.\frac{\partial u_c}{\partial y}\right|_{X_c}, \left.\frac{\partial^2 u_c}{\partial x^2}\right|_{X_c}, \left.\frac{\partial^2 u_c}{\partial y^2}\right|_{X_c}, \left.\frac{\partial^2 u_c}{\partial x \partial y}\right|_{X_c} \right]^{\mathbf{T}}. \tag{26}$$

In practical applications, it is preferable for the above residual function $B(u)$ to be minimized with respect to the partial derivatives $\boldsymbol{D}_u$, i.e.,

$$\frac{\partial B(u)}{\partial \{\boldsymbol{D}_u\}} = 0, \tag{27}$$

and the linear system of equations will be yielded as follows:

$$\boldsymbol{A}\boldsymbol{D}_{\boldsymbol{u}} = \boldsymbol{b}, \tag{28}$$

in which

$$\boldsymbol{A} = \begin{bmatrix} \sum_{k=1}^{m} w_k^2 h_k^2 & \sum_{k=1}^{m} w_k^2 h_k l_k & \sum_{k=1}^{m} w_k^2 \frac{h_k^3}{2} & \sum_{k=1}^{m} w_k^2 \frac{h_k l_k^2}{2} & \sum_{k=1}^{m} w_k^2 h_k^2 l_k \\ & \sum_{k=1}^{m} w_k^2 l_k^2 & \sum_{k=1}^{m} w_k^2 \frac{h_k^2 l_k}{2} & \sum_{k=1}^{m} w_k^2 \frac{l_k^3}{2} & \sum_{k=1}^{m} w_k^2 h_k l_k^2 \\ & & \sum_{k=1}^{m} w_k^2 \frac{h_k^4}{4} & \sum_{k=1}^{m} w_k^2 \frac{h_k^2 l_k^2}{4} & \sum_{k=1}^{m} w_k^2 \frac{h_k^3 l_k}{2} \\ & SYM & & \sum_{k=1}^{m} w_k^2 \frac{l_k^4}{4} & \sum_{k=1}^{m} w_k^2 \frac{h_k l_k^3}{2} \\ & & & & \sum_{k=1}^{m} w_k^2 h_k^2 l_k^2 \end{bmatrix}, \tag{29}$$

is the symmetric coefficient matrix, and the elements of matrix $\boldsymbol{A}$ are obtained based on the spatial coordinates of the node X_c and its neighboring nodes X_k. In addition,

$$\boldsymbol{b} = \begin{bmatrix} \sum_{k=1}^{m} u_k w_k^2 h_k - u_c \sum_{k=1}^{m} w_k^2 h_k \\ \sum_{k=1}^{m} u_k w_k^2 l_k - u_c \sum_{k=1}^{m} w_k^2 l_k \\ \sum_{k=1}^{m} u_k w_k^2 \frac{h_k^2}{2} - u_c \sum_{k=1}^{m} w_k^2 \frac{h_k^2}{2} \\ \sum_{k=1}^{m} u_k w_k^2 \frac{l_k^2}{2} - u_c \sum_{k=1}^{m} w_k^2 \frac{l_k^2}{2} \\ \sum_{k=1}^{m} u_k w_k^2 h_k l_k - u_c \sum_{k=1}^{m} w_k^2 h_k l_k \end{bmatrix}, \tag{30}$$

which depends on the numerical variables and spatial coordinates of nodes inside the star, moreover, can be decomposed as

$$\boldsymbol{b} = \boldsymbol{B}\boldsymbol{U}, \tag{31}$$

in which

$$\boldsymbol{B} = \left(-\sum_{k=1}^{m} w_k \boldsymbol{A}_2^{(k)}, w_1 \boldsymbol{A}_2^{(1)}, w_2 \boldsymbol{A}_2^{(2)}, \ldots, w_m \boldsymbol{A}_2^{(m)} \right)_{5\times(m+1)}, \tag{32}$$

$$\boldsymbol{U} = [u_c, u_1, u_2, \ldots, u_m]^T, \tag{33}$$

where

$$\boldsymbol{A}_2^{(k)} = \frac{w_k}{2}\left[2h_k, 2l_k, h_k^2, l_k^2, 2h_k l_k\right]^{\mathbf{T}}. \tag{34}$$

u_i $(i = c, 1, 2, 3, \ldots, m)$ represents the vector of function values at the node X_c and the other nodes X_k within the star. $\boldsymbol{D}_u$ can be described in an alternative form by merging Equation (28) with Equation (31) as follows:

$$\boldsymbol{D}_u = \boldsymbol{A}^{-1}\boldsymbol{b} = \boldsymbol{A}^{-1}(\boldsymbol{B}\boldsymbol{U}) = \boldsymbol{E}^c\boldsymbol{U}, \tag{35}$$

where

$$\boldsymbol{E}^c = \boldsymbol{A}^{-1}\boldsymbol{B}. \tag{36}$$

Drawing from the mathematical analysis provided, it is evident that for each central node X_c within the computational domain, the derivatives of the unknown function at point X_c can be approximated using a linear combination of the function values at the supporting nodes. Consequently, the partial derivatives at a central node can be articulated as follows:

$$\boldsymbol{D}_u = \begin{bmatrix} \frac{\partial u_c}{\partial x}\Big|_{X_c} \\ \frac{\partial u_c}{\partial y}\Big|_{X_c} \\ \frac{\partial^2 u_c}{\partial x^2}\Big|_{X_c} \\ \frac{\partial^2 u_c}{\partial y^2}\Big|_{X_c} \\ \frac{\partial^2 u_c}{\partial x \partial y}\Big|_{X_c} \end{bmatrix} = \begin{bmatrix} e_{1c}^c & e_{11}^c & e_{12}^c & \cdots & e_{1m}^c \\ e_{2c}^c & e_{21}^c & e_{22}^c & \cdots & e_{2m}^c \\ e_{3c}^c & e_{31}^c & e_{32}^c & \cdots & e_{3m}^c \\ e_{4c}^c & e_{41}^c & e_{42}^c & \cdots & e_{4m}^c \\ e_{5c}^c & e_{51}^c & e_{52}^c & \cdots & e_{5m}^c \end{bmatrix} \begin{bmatrix} u_c \\ u_1 \\ u_2 \\ \vdots \\ u_m \end{bmatrix}, \tag{37}$$

in which each element e_{ji}^c $(j = 1, 2, \ldots, 5; i = c, 1, 2, \ldots, m)$ of the matrix $\boldsymbol{E}^c$ can be derived by Equation (36). It is imperative to apply the above procedures at every node within the computational domain and along the boundary to develop equations that substitute for the spatial derivatives at each node. By ensuring compliance with boundary conditions at the boundary nodes and adherence to the governing equations at the interior nodes, a system of linear algebraic equations is derived as

$$\begin{bmatrix} \boldsymbol{E}_{1x} & \boldsymbol{E}_{1y} & \boldsymbol{E}_{1z} \\ \boldsymbol{E}_{2x} & \boldsymbol{E}_{2y} & \boldsymbol{E}_{2z} \\ \boldsymbol{E}_{3x} & \boldsymbol{E}_{3y} & \boldsymbol{E}_{3z} \end{bmatrix} \begin{bmatrix} \boldsymbol{U}_x^{all} \\ \boldsymbol{U}_y^{all} \\ \boldsymbol{U}_z^{all} \end{bmatrix} = \begin{bmatrix} \boldsymbol{F}_1 \\ \boldsymbol{F}_2 \\ \boldsymbol{F}_3 \end{bmatrix}, \tag{38}$$

and can be written in matrix form:

$$\boldsymbol{E}\boldsymbol{U}^{all} = \boldsymbol{F}. \tag{39}$$

Each matrix block in Equation (38) can be obtained from the above mathematical procedures. The numerical determination of function values at each node within the domain is accomplished by solving $\boldsymbol{U}^{all}$ in Equation (39).

4. Numerical Examples

In this section, to evaluate the performance of the proposed 2.5D GFDM, elastic wave problems with three different domains are analyzed. For all examples consisting of longitudinally invariant medium, the mechanical properties of the material correspond to a Young Modulus E of 156×10^9 Pa, a Poisson coefficient ν of 0.3, and a density ρ

of 2500 kg/m^3. The 3D approximations obtained using the 2.5D GFDM are contrasted with the exact solutions obtained from Green's functions for displacement in the three-dimensional frequency domain. The requisite Green's functions for various directionalities, as delineated by Lin [70], can be succinctly outlined as follows:

$$G_{xx} = A - B\gamma_x^2, \tag{40}$$

$$G_{yy} = A - B\gamma_y^2, \tag{41}$$

$$G_{zz} = A - B\gamma_z^2, \tag{42}$$

$$G_{xy} = G_{yx} = -B\gamma_x\gamma_y, \tag{43}$$

$$G_{xz} = G_{zx} = -B\gamma_x\gamma_z, \tag{44}$$

$$G_{yz} = G_{zy} = -B\gamma_y\gamma_z, \tag{45}$$

where

$$A = \frac{1}{4\pi\omega^2\rho}\left(k_s^2\frac{e^{-\mathrm{i}k_s r}}{r} - \left(\mathrm{i}k_s + \frac{1}{r}\right)\frac{e^{-\mathrm{i}k_s r}}{r^2} + \left(\mathrm{i}k_p + \frac{1}{r}\right)\frac{e^{-\mathrm{i}k_p r}}{r^2}\right), \tag{46}$$

$$B = \frac{1}{4\pi\omega^2\rho}\left(\left(k_s^2 - \frac{3}{r^2} - \frac{3\mathrm{i}k_s}{r}\right)\frac{e^{-\mathrm{i}k_s r}}{r} - \left(k_p^2 - \frac{3}{r^2} - \frac{3\mathrm{i}k_p}{r}\right)\frac{e^{-\mathrm{i}k_p r}}{r}\right), \tag{47}$$

in which $k_s = \sqrt{\omega^2\rho/\mu}$, $k_p = \sqrt{\omega^2\rho/(\lambda+2\mu)}$, $\gamma_j = \partial r/\partial x_j = x_j/r$ with $j = x, y, z$, and r stands for the three-dimensional distance between the source and field points. A point source is located at (x_s, y_s, z_s). The analytical solutions of the problem in the frequency-wavenumber domain can be expressed in the subsequent format:

$$\overline{u}_x = G_{xx} + G_{xy} + G_{xz}, \tag{48}$$

$$\overline{u}_y = G_{yx} + G_{yy} + G_{yz}, \tag{49}$$

$$\overline{u}_z = G_{zx} + G_{zy} + G_{zz}. \tag{50}$$

Furthermore, to assess the precision of the proposed methodology, the global error (Gerr) and the normalized error (Nerr) serve as pivotal metrics, employed as follows:

$$\mathrm{Gerr}(\phi) = \sqrt{\frac{\sum_{i=1}^{N}\left[\phi_e(X_i) - \phi_n(X_i)\right]^2}{\sum_{i=1}^{N}\left[\phi_e(X_i)\right]^2}}, \tag{51}$$

$$\mathrm{Nerr}[\phi_n(X_i)] = \frac{|\phi_e(X_i) - \phi_n(X_i)|}{\max\limits_{x\in\Omega}|\phi_e(X_i)|}, \tag{52}$$

where the variable X_i denotes the i^{th} calculation point, while N represents the total count of calculation points, $\phi_e(X_i)$ and $\phi_n(X_i)$ correspond to the exact and numerical outcomes, respectively, at the i^{th} calculation point.

Example 1. *We first consider a three-dimensional model that is infinitely extended in the z-direction, featuring a square cross-section, covering $0 \le x, y \le 1$. The geometry and parameters are invariant along the z-axis, as shown in Figure 2.*

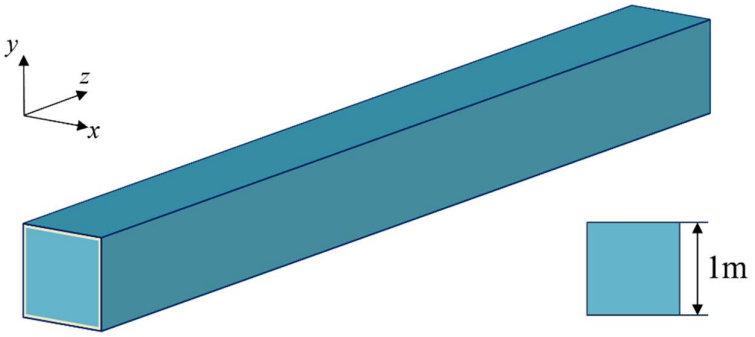


Figure 2. A three-dimensional model with a square cross-section and invariant geometry along the z-direction.

The interior nodes are uniformly distributed within the computational domain, and the same applies to the boundary nodes, as illustrated in Figure 3. The Dirichlet boundary conditions shown as Equation (6) are applied to the four edges of the square cross-section, where $\mathbf{u}_b$ is a vector comprising the components $\overline{u}_x$, $\overline{u}_y$, and $\overline{u}_z$. The boundary conditions will be transformed into 2.5D Dirichlet boundary conditions applicable to Equation (20) by performing the spatial Fourier transforms along the z-direction. In this case, the value of m is set to 12. The points source is located at $(-1.5, -1.5,\ 0)$, oscillating with a frequency of f.

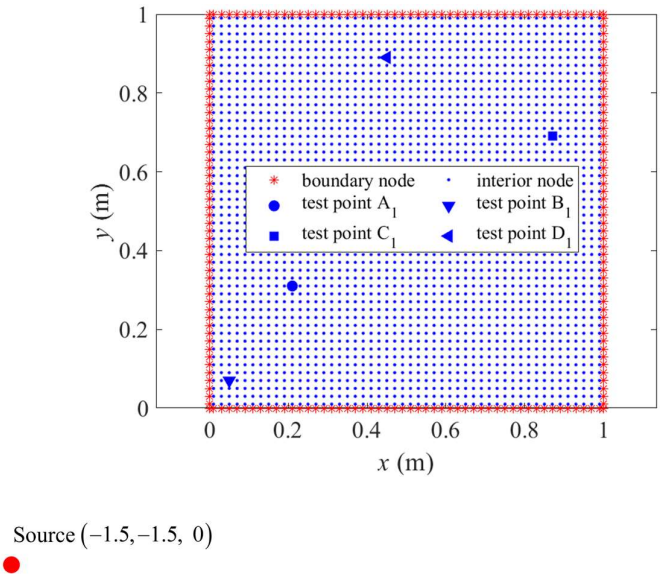


Figure 3. A schematic representation of uniform distribution of interior nodes and boundary nodes, along with a source point and test points for Example 1.

Before solving three-dimensional problems, it is essential to verify the applicability of the GFDM prior to applying the inverse spatial Fourier transform to the frequency-wavenumber domain results. The test point A_1 located at $(0.21,\ 0.31)$ is selected to assess the accuracy of GFDM in the frequency-wavenumber domain. Figure 4 presents the real and imaginary parts of the displacement at the test point and the normalized error (Nerr) between numerical solutions and analytical solutions at the frequency of 1500 Hz. This analysis covers a wavenumber range from -10 rad/m to 10 rad/m, sampled at linearly spaced intervals with increased density near $\pm k_p$ and $\pm k_s$, encompassing a total of 2704 points, including 204 boundary points and 2500 interior points. The analytical solutions of this problem can be expressed by

$$u_x^{2.5D} = \frac{1}{4\mathrm{i}\rho\omega^2}\left[k_s^2 H_{0\beta} - \frac{1}{r_{2D}}B_1 + \eta_x^2 B_2 + \eta_x\eta_y B_2 + \mathrm{i}k_z\eta_x B_1\right], \tag{53}$$

$$u_y^{2.5D} = \frac{1}{4i\rho\omega^2}\left[k_s^2 H_{0\beta} - \frac{1}{r_{2D}}B_1 + \eta_y^2 B_2 + \eta_x\eta_y B_2 + ik_z\eta_y B_1\right], \tag{54}$$

$$u_z^{2.5D} = \frac{1}{4i\rho\omega^2}\left[k_s^2 H_{0\beta} - k_z^2 B_0 + ik_z\eta_x B_1 + ik_z\eta_y B_1\right], \tag{55}$$

with $B_n = k_\beta^n H_{n\beta} - k_\alpha^n H_{n\alpha}$, $k_\alpha = \sqrt{k_p^2 - k_z^2}$ with $\mathrm{Im}(k_\alpha) < 0$, $k_\beta = \sqrt{k_s^2 - k_z^2}$ with $\mathrm{Im}(k_\beta) < 0$, $\eta_I = \partial r_{2D}/\partial x_I = x_I/r_{2D}$ with $I = x, y$, $H_{n\alpha} = H_n^{(2)}(k_\alpha r_{2D})$, $H_{n\beta} = H_n^{(2)}(k_\beta r_{2D})$, where the function $H_n^{(2)}$ represents the Hankel function of the second kind and of the n^{th} order, while r_{2D} denotes the two-dimensional distance between the source and the field points.

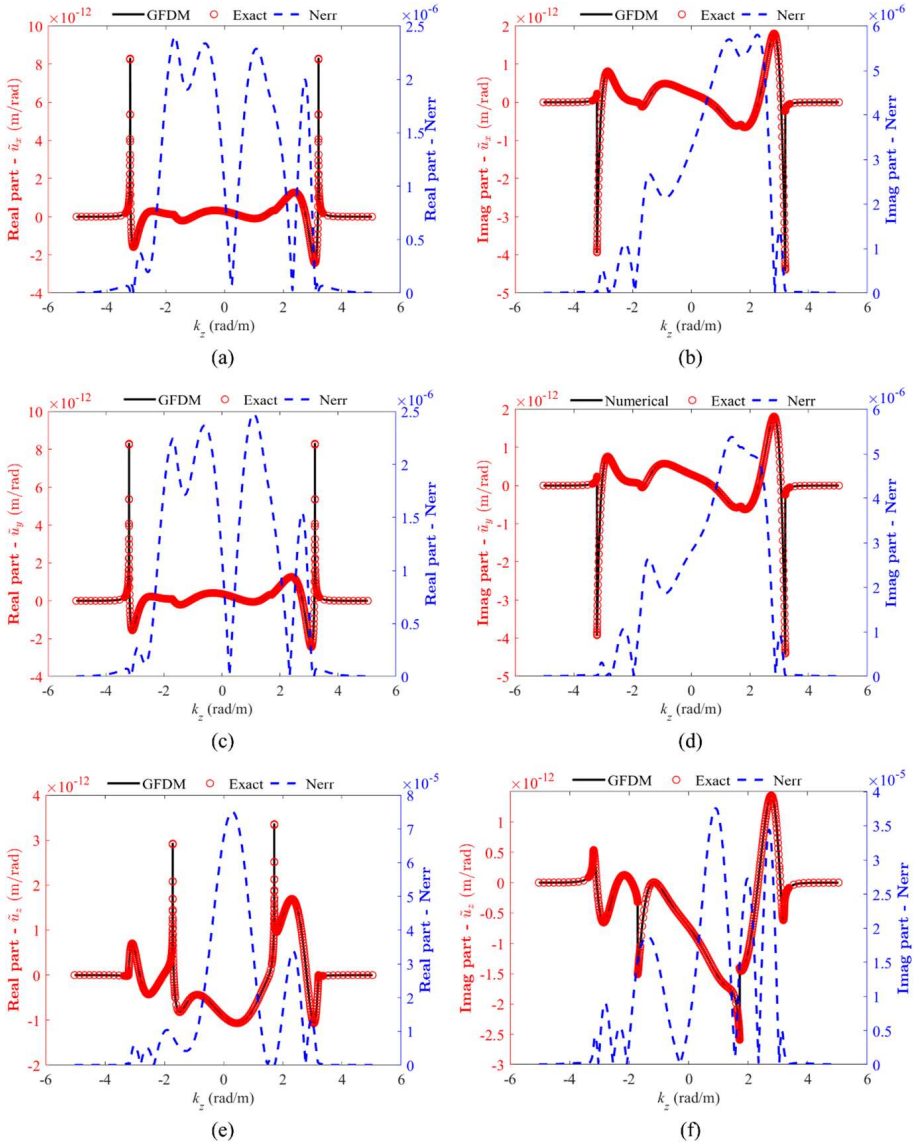


Figure 4. Solutions of displacements by the GFDM at the test point A_1 with the frequency of 2500 Hz: (**a**,**c**,**e**) represent real parts of $\tilde{u}_x$, $\tilde{u}_y$, $\tilde{u}_z$, respectively, and the normalized errors between numerical and analytical solutions; (**b**,**d**,**f**) represent imaginary parts of, $\tilde{u}_x$ $\tilde{u}_y$, $\tilde{u}_z$, respectively, and the normalized errors between numerical and analytical solutions.

It can be observed that in the frequency-wavenumber domain, the numerical solutions obtained from the GFDM for displacements in three directions align well with the exact solutions. Consequently, the GFDM is capable of effectively addressing the propagation of elastic waves in the frequency-wavenumber domain.

To demonstrate the distinctive features of GFDM, the above problem was analyzed using non-uniformly distributed interior nodes and boundary nodes, as shown in Figure 5, specifically showcasing an instance of randomly arranged nodal points. Under identical parametric configurations, Figure 6 presents the real and imaginary parts of the displacement at the test point and Nerr between numerical solutions and analytical solutions with randomly distributed interior nodes and boundary nodes.

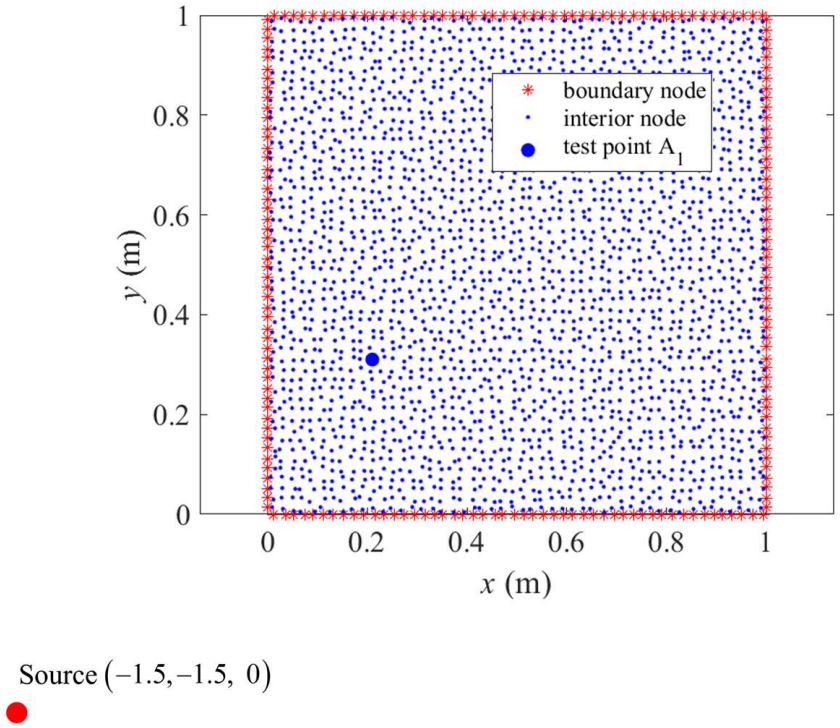


Figure 5. A schematic representation of non-uniform distribution of interior nodes and boundary nodes for Example 1.

Comparative analysis of Figures 4 and 6 reveals that while non-uniform nodal configurations induce a marginal elevation in normalized errors relative to uniform distributions, the accuracy remains acceptable.

In order to ascertain the integration limits for the inverse Fourier transform, the numerical results of the exact solution $u_y^{2.5D}$ are obtained by assigning values to the magnitude of k_z. Due to the presence of the Hankel function, $u_y^{2.5D}$ begins to decay rapidly at $|k_z| = k_s$. Specifically, when $k_z = -k_s$, $u_y^{2.5D}$ takes the value of $1.46 \times 10^{-14} - 4.99 \times 10^{-13}$i; when $k_z = k_s$, it takes the value of $3.97 \times 10^{-13} - 7.96 \times 10^{-13}$i. As k_z is further extended to $-3k_s$ and $3k_s$, $u_y^{2.5D}$ exhibits a monotonic decrease to $1.82 \times 10^{-17} + 5.43 \times 10^{-17}$i. To achieve a balance between precision and efficiency, the integration limits were judiciously defined as $[-\gamma k_s,\ \gamma k_s]$, with γ set to 4. Subsequent to performing the inverse Fourier transform on $u_y^{2.5D}$, the relative error between the computed outcome and $\overline{u}_y$ was meticulously calculated to be 2.16×10^{-4}, representing that the computational error associated with the chosen integration limits is adequate to satisfy the precision demands for subsequent computational analyses.

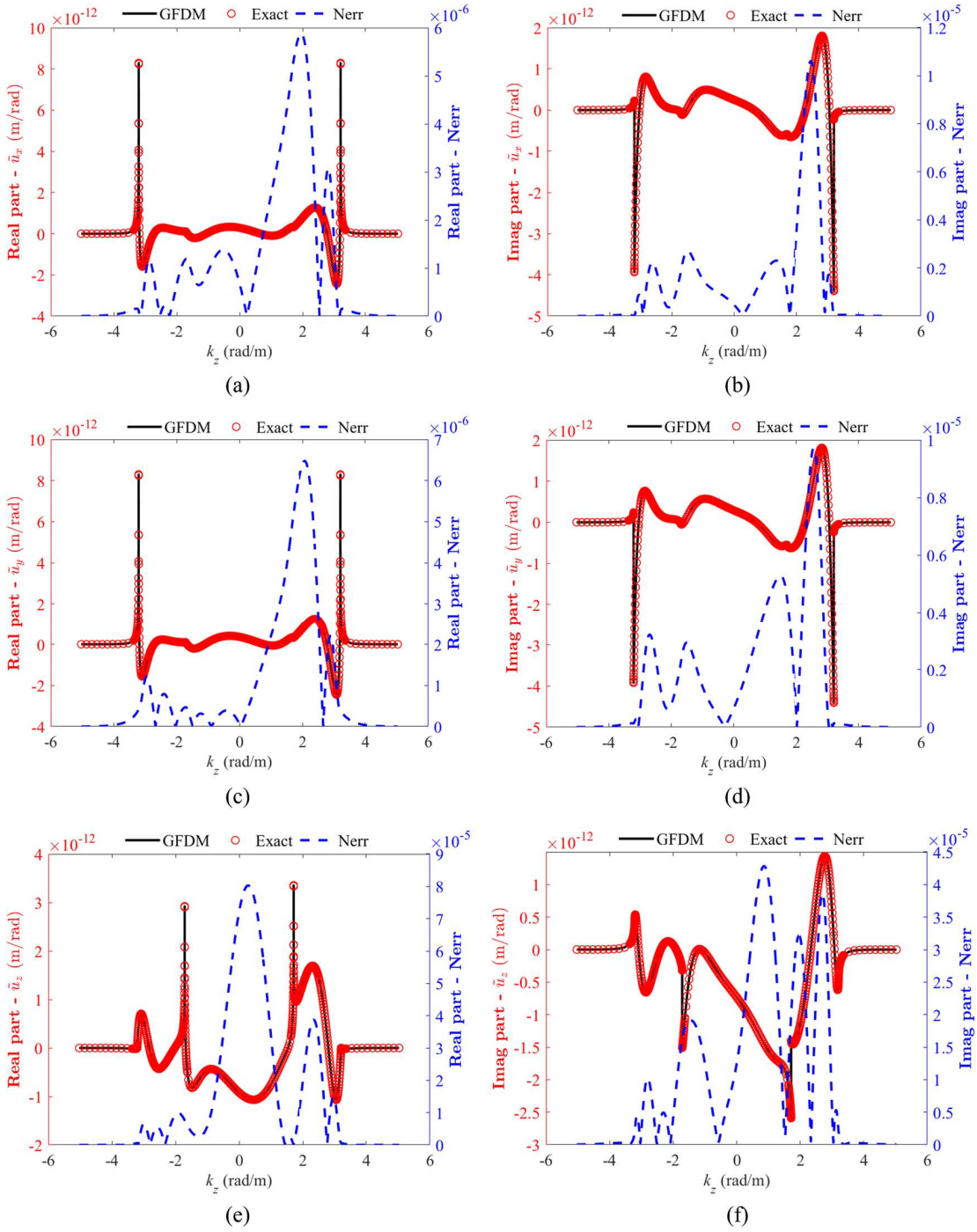


Figure 6. Solutions of displacements by the GFDM, with non-uniformly distributed interior nodes and boundary nodes, at the test point A_1 with the frequency of 2500 Hz: (**a**,**c**,**e**) represent real parts of $\widetilde{u}_x$, $\widetilde{u}_y$, $\widetilde{u}_z$, respectively, and the normalized errors between numerical and analytical solutions; (**b**,**d**,**f**) represent imaginary parts of, $\widetilde{u}_x$, $\widetilde{u}_y$, $\widetilde{u}_z$, respectively, and the normalized errors between numerical and analytical solutions.

After applying an inverse spatial Fourier transform along the z-direction to the results in the frequency-wavenumber domain, we can obtain the 3D numerical solution for Example 1. Figure 7 shows the global error for the amplitude of three-dimensional displacements u_z, obtained from 2.5D GFDM, at different frequencies with respect to the total number of nodes. As it is illustrated in Figure 7, the 2.5D GFDM demonstrates stable convergence to the exact solutions. Table 1 presents the global errors for the amplitude of three-dimensional displacements u_z obtained from different node distributions of 2.5D GFDM under varying

numbers of nodes at 3000 Hz. Through comparative analysis, as the number of nodes increases, the errors generated by random node distribution converge with those from uniform distribution, demonstrating the robustness of 2.5D GFDM while indicating that stochastic nodal arrangements exert no significant influence on computational outcomes.

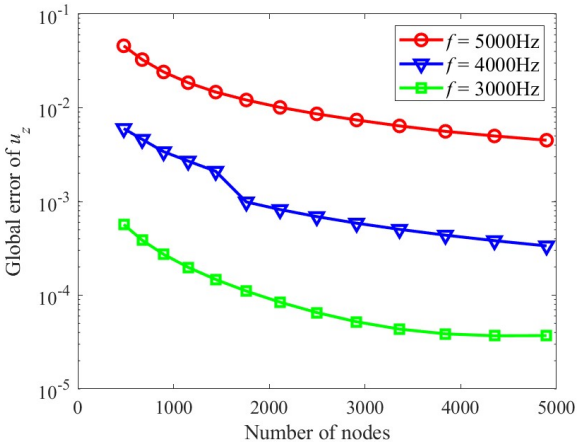


Figure 7. Global errors for the amplitude of three-dimensional displacement u_z at different frequencies of 3000 Hz, 4000 Hz and 5000 Hz with respect to the total number of nodes.

Table 1. Global errors for u_z obtained from different node distributions under varying numbers of nodes at 3000 Hz.

Number of Nodes	Global Errors	
	Uniform Distribution	Non-Uniform Distribution
1020	2.3220×10^{-4}	3.1495×10^{-4}
1365	1.5837×10^{-4}	1.9652×10^{-4}
1760	1.1066×10^{-4}	1.5055×10^{-4}

Table 2 presents the influence of different values of m (with a fixed node count of 2704) on the results of 2.5D GFDM at 3000 Hz and 4000 Hz. The data demonstrate that the numerical accuracy of the 2.5D GFDM exhibits low sensitivity to the variation of m-values. Notably, for a given number of nodes, arbitrarily increasing the values of m was found to adversely affect computational precision. Based on these findings, m = 12 was adopted for all subsequent analyses to balance efficiency and accuracy.

Table 2. Global errors and time costs for u_z with varying m-values under 2704 nodes.

Frequency	Number of m	Global Errors	Time
3000 Hz	12	3.3319×10^{-4}	316 s
	18	4.0470×10^{-4}	330 s
	25	6.0844×10^{-4}	342 s
4000 Hz	12	1.2688×10^{-3}	320 s
	18	1.6112×10^{-3}	331 s
	25	2.4420×10^{-3}	358 s

To validate the efficiency of the 2.5D GFDM method at the frequencies of 3000 Hz and 4000 Hz, we calculated the amplitude of 3D displacements u_z on the xy plane at $z = 0$ m using the 2.5D GFDM, recorded the computation time, and evaluated the global errors between the 2.5D GFDM results and the exact solution. The computation time and global error were then compared with those obtained from the 3D FEM combined with Perfectly

Matched Layer (PML) in COMSOL Multiphysics® 6.3, as shown in Table 3. The results demonstrate that the 2.5D GFDM outperforms traditional 3D numerical methods in both efficiency and accuracy.

Table 3. Global errors and computation time for u_z obtained from 2.5D GFDM and 3D FEM-PML.

Frequency	2.5D GFDM			3D FEM-PML		
	Number of Nodes	Global Errors	Time	Number of Units	Global Errors	Time
3000 Hz	1020	8.9959×10^{-4}	46 s	187,322	2.4157×10^{-3}	52 s
4000 Hz	2205	1.5428×10^{-4}	243 s	784,280	5.7978×10^{-2}	378 s

In the following, to investigate the performance of the proposed method in calculating the xy plane, we selected the plane at $z = 5$ m for frequencies of 2500 Hz and 3250 Hz, another plane at $z = 2$ m for a frequency of 4000 Hz, respectively. The normalized errors of these three cases are illustrated in Figures 8–10. It can be observed that the 2.5D GFDM maintains a high level of accuracy when calculating the three-dimensional displacement fields on the xy planes at various positions along the z-axis. Furthermore, the proposed method demonstrates higher accuracy in calculating the displacement fields u_x and u_y at lower frequencies.

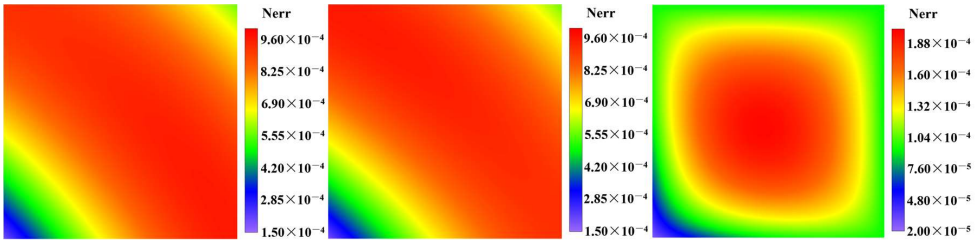


Figure 8. The normalized errors of the amplitude of displacement fields (**a**) u_x, (**b**) u_y, and (**c**) u_z on the xy plane at $z = 5$ m for Example 1 with a frequency of 2500 Hz.

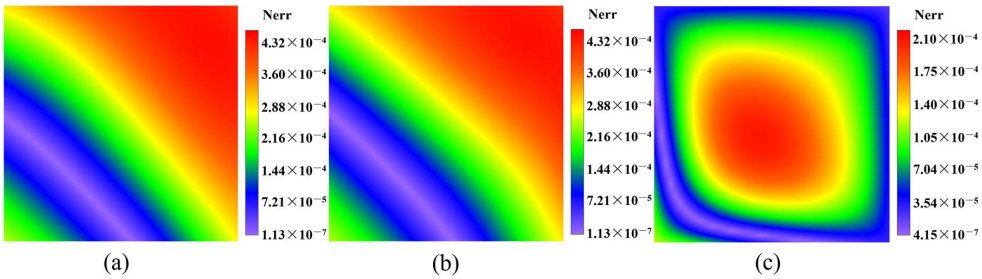


Figure 9. The normalized errors of the amplitude of displacement fields (**a**) u_x, (**b**) u_y, and (**c**) u_z on the xy plane at $z = 5$ m for Example 1 with a frequency of 3250 Hz.

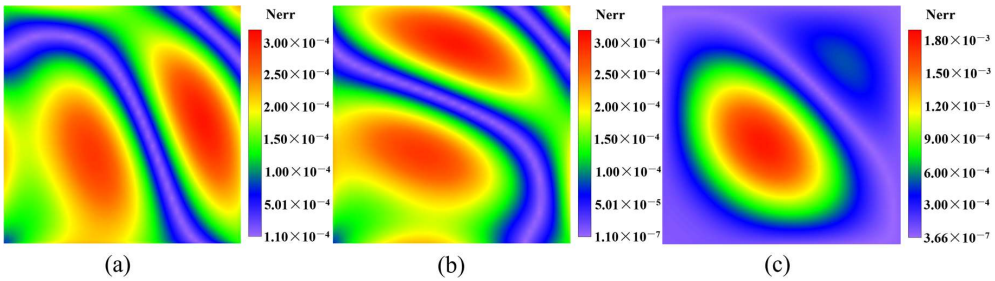


Figure 10. The normalized errors of the amplitude of displacement fields (**a**) u_x, (**b**) u_y, and (**c**) u_z on the xy plane at $z = 2$ m for Example 1 with a frequency of 4000 Hz.

Furthermore, we study the performance of the proposed method in calculating the propagation of displacements along the z-axis. In Example 1, we selected three test points located at $B_1(0.05, 0.07)$, $C_1(0.87, 0.69)$, and $D_1(0.45, 0.89)$ within the computational domain, as shown in Figure 3, examining the propagation of displacement from -10 m to 10 m along the z-axis at a frequency of 4000 Hz. Figures 11–13 illustrate the approximated solutions and exact solutions of u_x, u_y and u_z for this scenario, as well as their normalized errors, which demonstrate that the proposed method exhibits commendable accuracy in the computation of elastic wave propagation along the z-axis within the medium at higher frequencies.

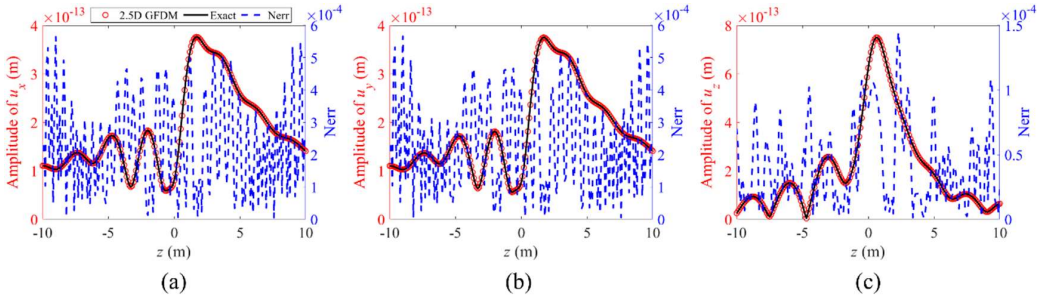


Figure 11. The propagation of displacements (**a**) u_x, (**b**) u_y, and (**c**) u_z, and normalized errors between numerical solutions and exact solutions for point $B_1(0.05, 0.07)$ from -10 m to 10 m along the z-axis at a frequency of 4000 Hz, in Example 1.

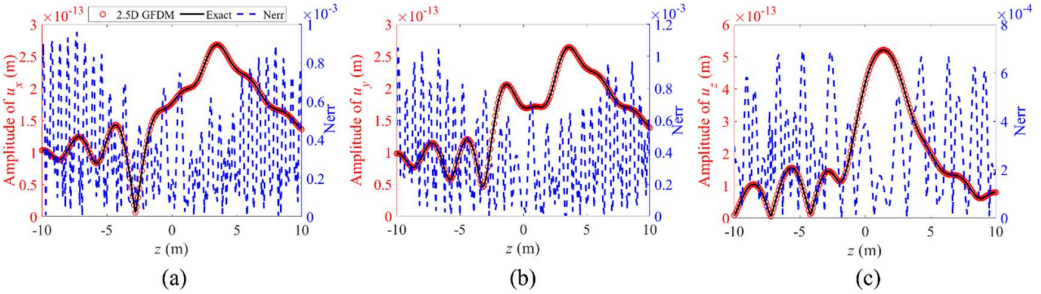


Figure 12. The propagation of displacements (**a**) u_x, (**b**) u_y, and (**c**) u_z and normalized errors between numerical solutions and exact solutions for point $C_1(0.87, 0.69)$ from -10 m to 10 m along the z-axis at a frequency of 4000 Hz, in Example 1.

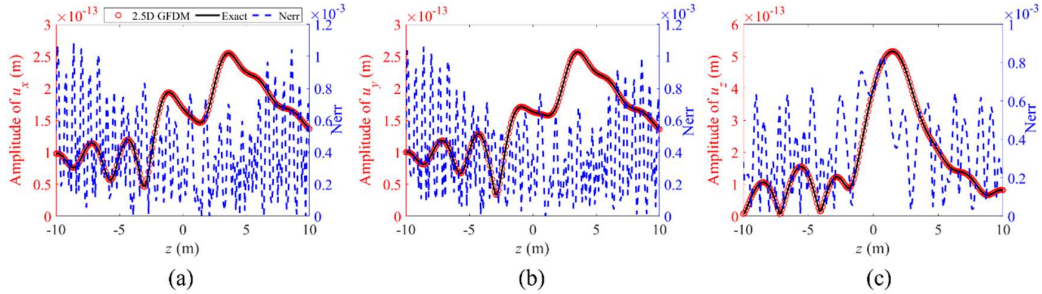


Figure 13. The propagation of displacements (**a**) u_x, (**b**) u_y, and (**c**) u_z and normalized errors between numerical solutions and exact solutions for point $D_1(0.45, 0.89)$ from -10 m to 10 m along the z-axis at a frequency of 4000 Hz, in Example 1.

Example 2. *In this example, we consider a cylindrical model that is infinitely extended in the z-direction with a circular cross-section, where the circle is centered at the origin point (0, 0, 0) with a radius of 1 m, as depicted in Figure 14. The three-dimensional model parameters remain constant along the z-direction with the same point source as Example 1.*

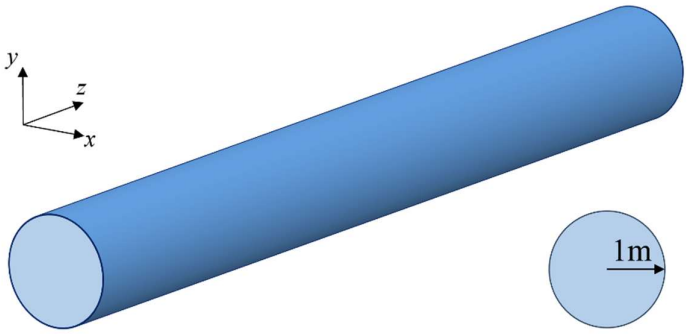


Figure 14. A cylindrical model with a circular cross-section and invariant geometry along the z-direction.

A total of 2116 nodes, including 148 boundary nodes and 1968 interior nodes, are uniformly distributed across both the interior and the boundary of the domain, as shown in Figure 15 (not to scale). Mixed boundary conditions are applied at the boundary nodes. For the upper half of the model's boundary, Dirichlet boundary conditions are applied, whereas Neumann boundary conditions are imposed on the lower half of the boundary. $\mathbf{t}_b$ is a vector comprising the three components of traction. It is necessary to perform the spatial Fourier transforms along the z-direction on both Dirichlet boundary conditions and Neumann boundary conditions to derive their 2.5D form applicable to this example. The three-dimensional numerical solutions derived from the 2.5D GFDM are compared with the exact solutions given by Equations (48)–(50).

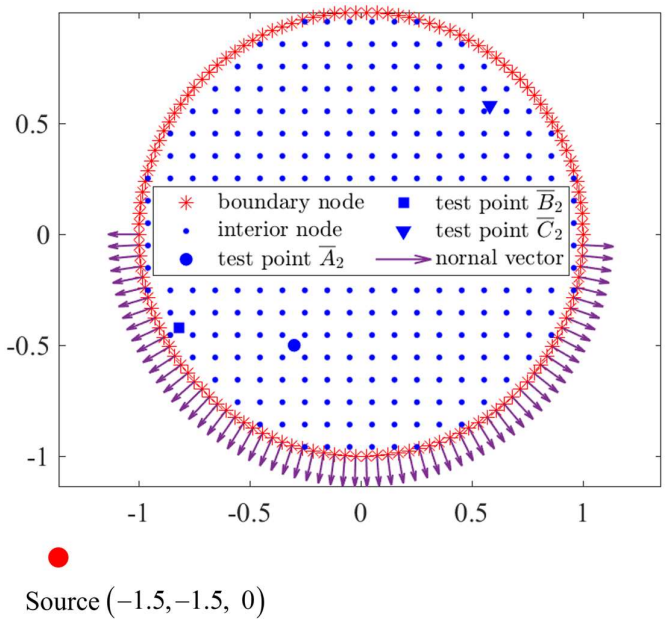


Figure 15. A schematic representation of uniform distribution of interior nodes, boundary nodes, along with a source point and test points for Example 2.

The performance of the proposed method is explored in calculating this example. Figure 16 depicts contour plots of the amplitude of displacement fields on the xy plane $z = 2$ m for the problem at the frequency of 2500 Hz. The upper part of the figure represents the computational results obtained utilizing the 2.5D GFDM introduced in this research. These results are compared with those on the lower part, which exhibits the displacement fields derived from the exact analytical solutions. It is apparent that there is an exact correspondence between the two parts of the figures.

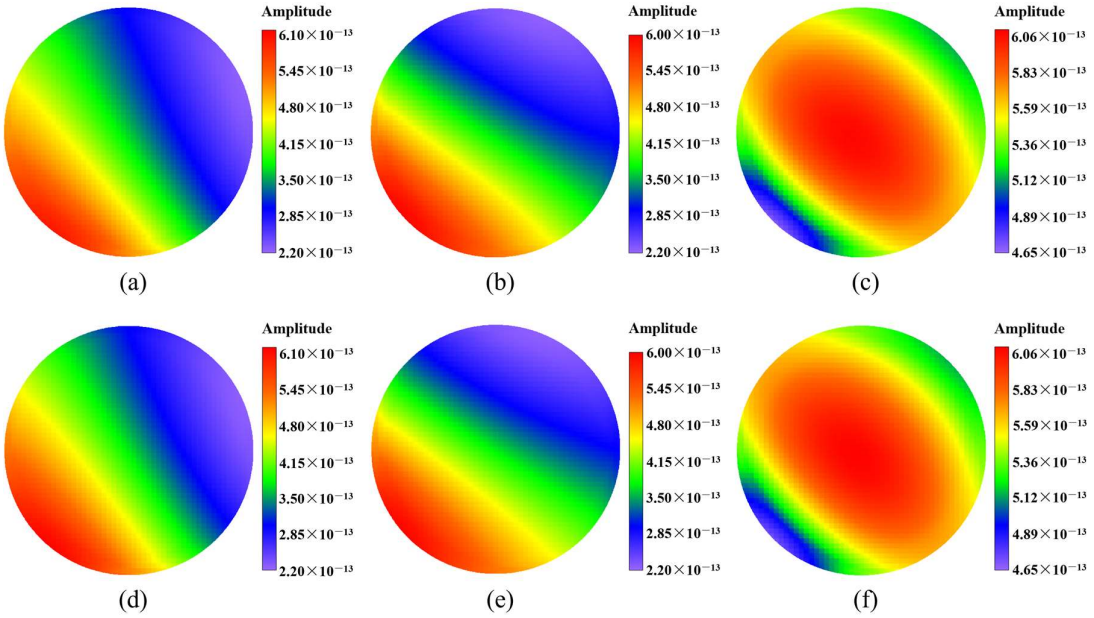


Figure 16. The contour plots of displacement fields at 2250 Hz on the plane $z = 2$ m in Example 2 computed by the 2.5D GFDM and the exact solutions: (**a**–**c**) represent numerical solutions of amplitude of displacement u_x, u_y, and u_z, respectively; (**d**–**f**) represent exact solutions of amplitude of displacement u_x, u_y, and u_z, respectively.

Moreover, Figures 17 and 18 display color maps calculated under conditions analogous to those in Figure 16, but for the xy planes of $z = 0.5$ m and $z = 1$ m with excitation frequencies of 3250 Hz and 4000 Hz, respectively. Consistent with the previous figure, a precise correspondence is observed between the outcomes yielded by the numerical method and exact solutions.

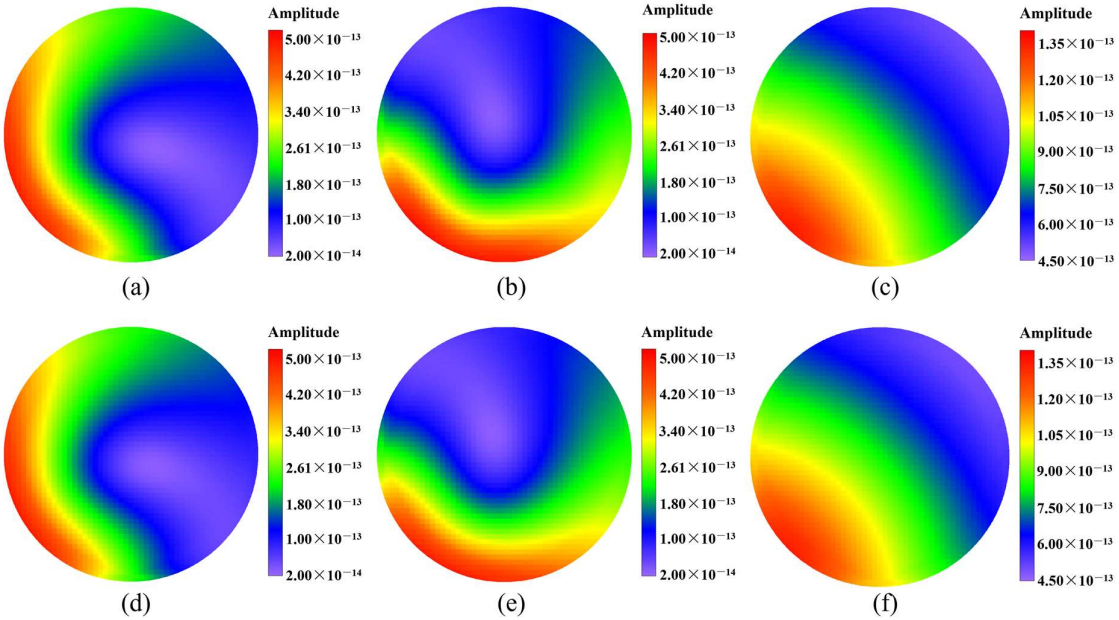


Figure 17. The contour plots of displacement fields at 3250 Hz on the plane $z = 0.5$ m for Example 2, computed by the 2.5D GFDM and the exact solutions: (**a**–**c**) represent numerical solutions of amplitude of displacement u_x, u_y, and u_z, respectively; (**d**–**f**) represent exact solutions of amplitude of displacement u_x, u_y, and u_z, respectively.

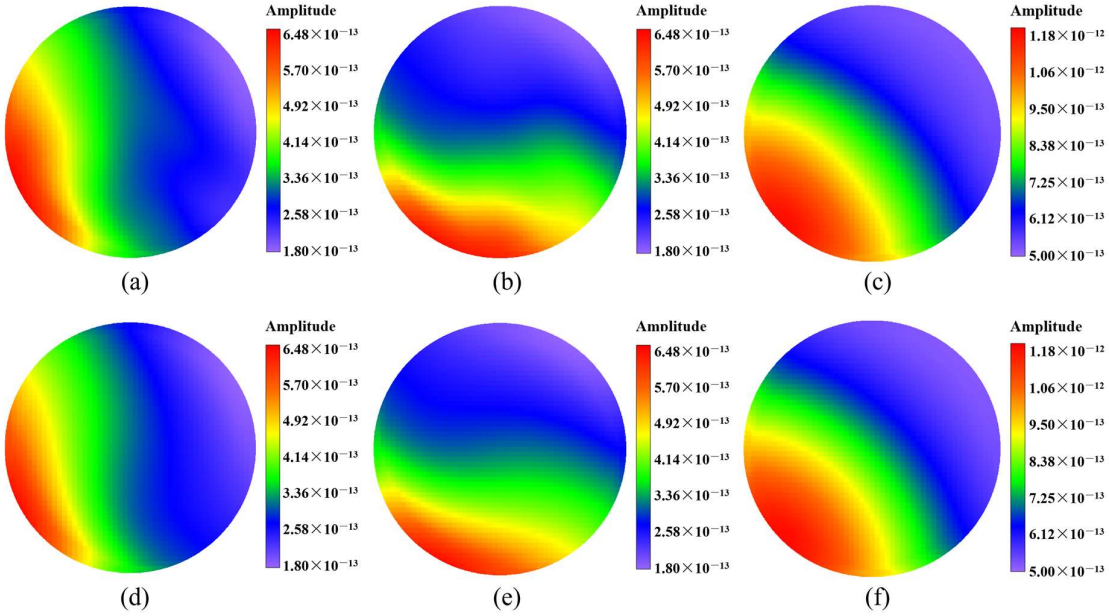


Figure 18. The contour plots of displacement fields at 4000 Hz on the plane $z = 1$ m for Example 2, computed by the 2.5D GFDM and the exact solutions: (**a**–**c**) represent numerical solutions of amplitude of displacement u_x, u_y, and u_z, respectively; (**d**–**f**) represent exact solutions of amplitude of displacement u_x, u_y, and u_z, respectively.

In the following, the accuracy of the method in calculating the propagation of displacements along the z-axis is assessed with respect to its application to Example 2. Figures 19–21 exhibit the propagation of displacement in three directions and the normalized errors between the approximated solutions and the exact solutions of three test points from -10 m to 10 m along the z-direction with a source frequency of 2250 Hz. The test points are selected at $\overline{A}_2$ $(-0.3, -0.5)$, $\overline{B}_2$ $(-0.82, 0.42)$, and $\overline{C}_2$ $(0.58, 0.58)$, as shown in Figure 15, within the computational domain. From the figures, it can be observed that the normalized error primarily maintains an amplitude around 10^{-4}, once again demonstrating that this method retains robustness when calculating the propagation of displacement in the z-direction, which indicates that this method is capable of accurately predicting the displacement fields at the frequency for this example.

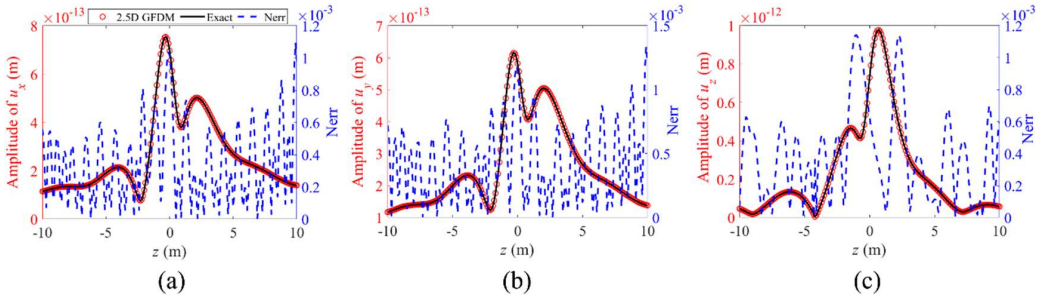


Figure 19. The propagation of displacements (**a**) u_x, (**b**) u_y, and (**c**) u_z, and normalized errors between numerical solutions and exact solutions for point $\overline{A}_2(-0.3, -0.5)$ from -10 m to -10 m along the z-axis at a frequency of 2250 Hz, in Example 2.

In Figures 22 and 23, the real and imaginary parts of displacements u_y and u_z against the frequencies ranging from 500 to 4000 Hz, as derived from both 2.5D GFDM and exact solutions at the receiving points $B_2(-0.82, 0.42, 1)$ and $C_2(0.58, 0.58, 1)$, are depicted. A close correspondence between the outcomes of the proposed method and analytical solutions at the considered frequencies can be evidently observed.

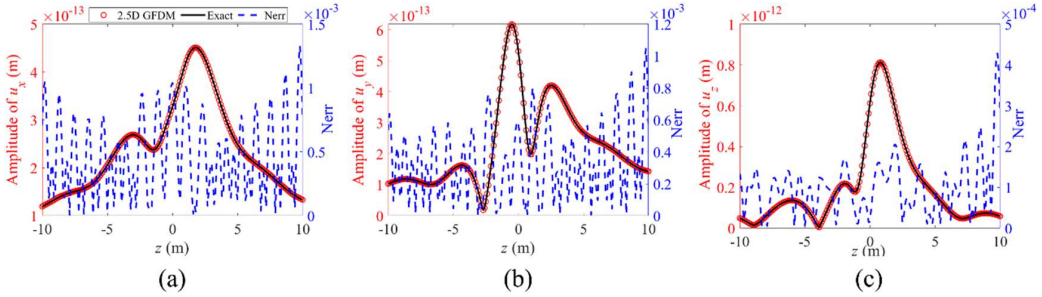


Figure 20. The propagation of displacements (**a**) u_x, (**b**) u_y, and (**c**) u_z, and normalized errors between numerical solutions and exact solutions for point $\overline{B}_2(-0.82, 0.42)$ from -10 m to -10 m along the z-axis at a frequency of 2250 Hz, in Example 2.

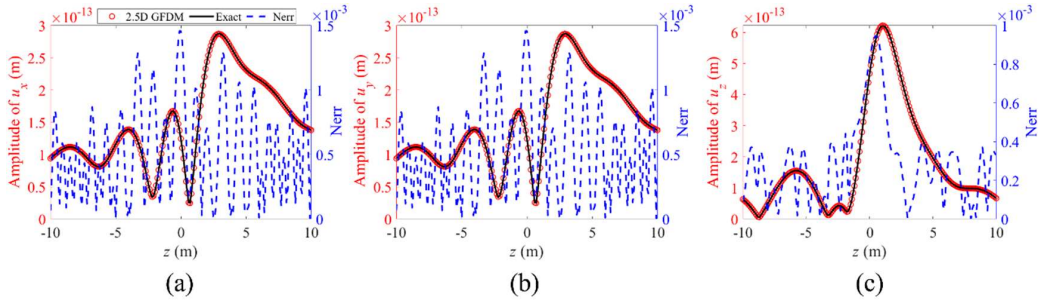


Figure 21. The propagation of displacements (**a**) u_x, (**b**) u_y, and (**c**) u_z, and normalized errors between numerical solutions and exact solutions for point $\overline{C}_2(0.58, 0.58)$ from -10 m to -10 m along the z-axis at a frequency of 2250 Hz, in Example 2.

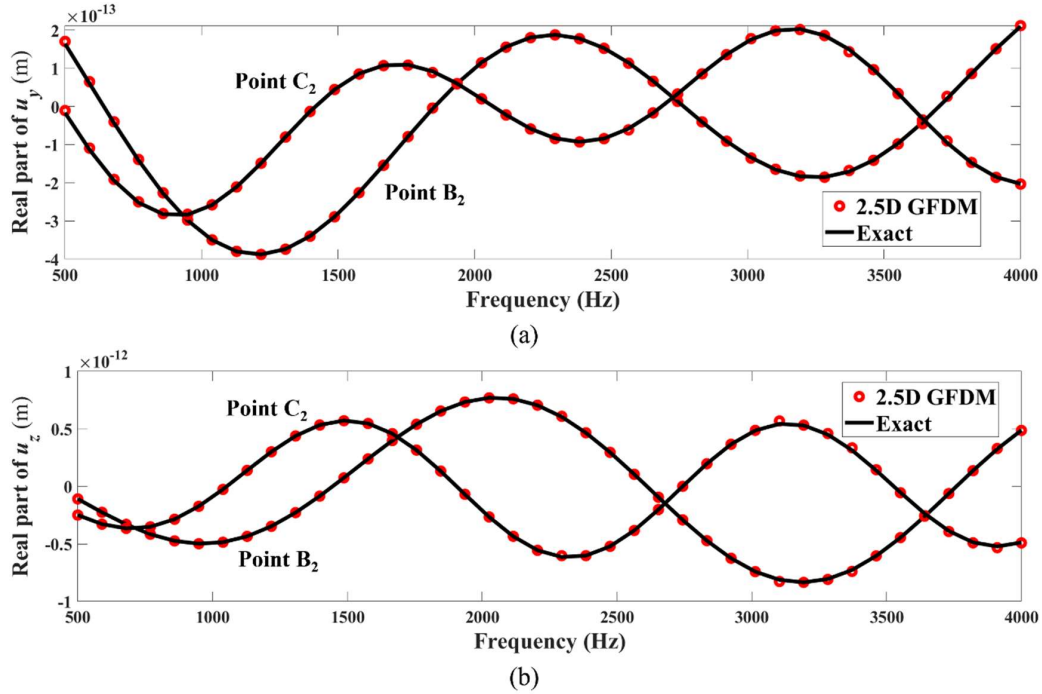


Figure 22. Real parts of frequency response of displacements (**a**) u_y and (**b**) u_z at test points $B_2(-0.82, 0.42, 1)$ and $C_2(0.58, 0.58, 1)$ in Example 2, computed by 2.5D GFDM and analytical solutions.

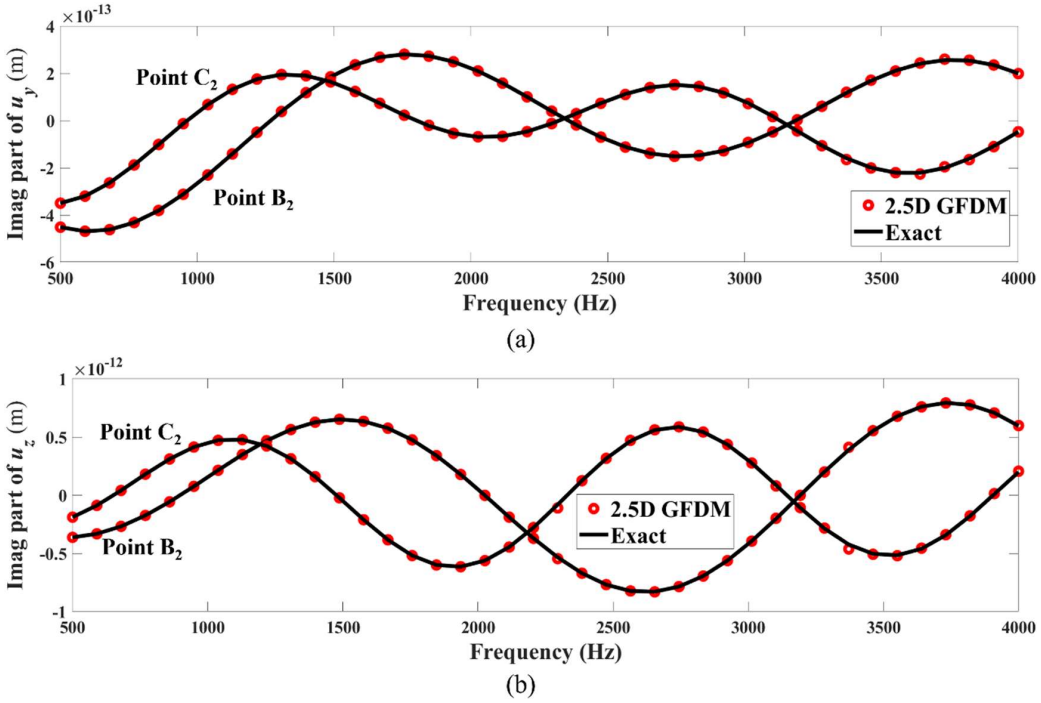


Figure 23. Imaginary parts of frequency response of displacements (**a**) u_y and (**b**) u_z at test points $B_2(-0.82, 0.42, 1)$ and $C_2(0.58, 0.58, 1)$ in Example 2, computed by 2.5D GFDM and analytical solutions.

Example 3. *To further validate the performance of the method related to engineering applications, a tunnel structure infinitely extended in the z-direction with an annular cross-section, centered at the origin, is examined, where the external radius is 3.0 m and the inner radius is 2.75 m, with a medium of 0.25 m thickness filling the space between the two radii. The medium of the tunnel and its cross-sectional geometry remain constant along the z-direction, as illustrated in Figure 24.*

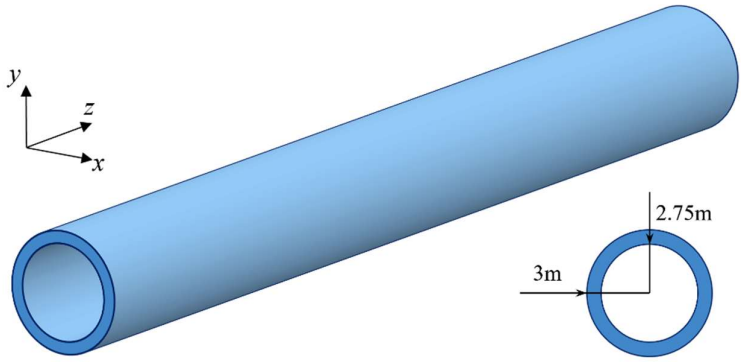


Figure 24. An infinitely long tunnel structure with an annular cross-section and invariant geometry along the z-direction.

The nodes, consisting of 180 inner boundary points, 197 outer boundary points, and 1832 interior nodes between them, are uniformly distributed across both the interior and the boundary of the domain, as shown in Figure 25. The Dirichlet boundary conditions shown as Equation (6) are imposed on the entire inner boundary of the tunnel, while Neumann boundary conditions are applied to the outer boundary. Consistent with Example 2, a spatial Fourier transform along the z-direction shall be performed on both boundary conditions to derive their 2.5D form applicable to this example. In the first case of Example 3, we consider a source point positioned outside the entire tunnel structure, specifically at $(0, -4, 0)$.

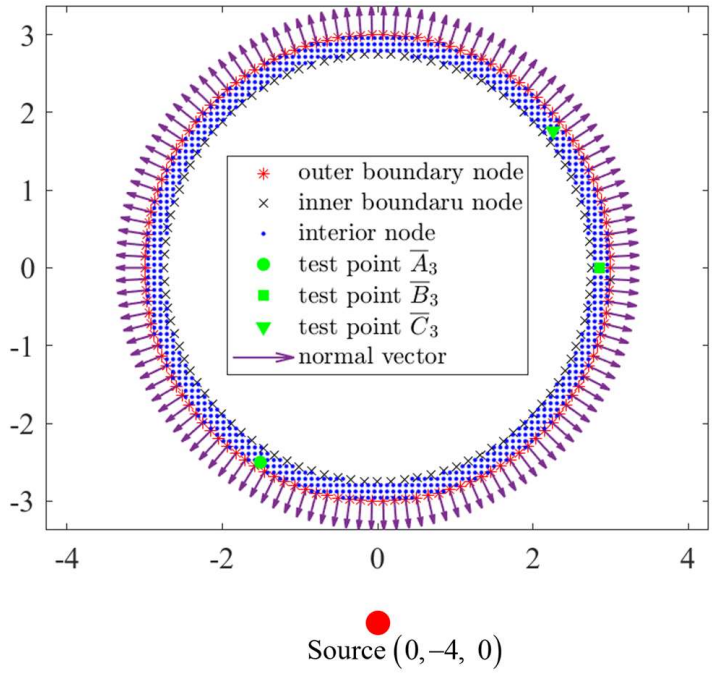


Figure 25. A schematic representation of uniform distribution of interior nodes and boundary nodes, along with an outer source point and test points for Example 3.

Figure 26 presents contour plots illustrating the amplitude of the displacement field on the xy plane at $z = 3$ m for the problem at the frequency of 2250 Hz. The left-hand section of the figure shows the outcomes of calculations using the 2.5D GFDM. These outcomes are juxtaposed with the central section, which displays displacement fields derived from analytical solutions. The right-hand section of the figure provides contour plots of the normalized errors between the left and central sections. Additionally, in the map of normalized errors, it is observable that for the displacement fields in three directions, only a very small portion of the normalized errors is on the order of 10^{-3}, while the remaining normalized errors are on the order of 10^{-4}, demonstrating a high level of agreement. This indicates that the 2.5D GFDM is effective in computing displacement fields for tunnel structures with thinner walls. In addition, Figures 27 and 28 exhibit chromatic representations computed under conditions parallel to those in Figure 26, yet for the planes at $z = 5$ m and $z = 1$ m, with excitation frequencies of 3250 Hz and 4000 Hz, respectively. Aligning with the preceding figure, a congruence is discerned between the numerical outcomes and the analytical solutions. It should be noted that the regions with higher errors in the map of normalized errors are results of the differences in the distribution of grid points between the computational domain and the boundaries during the discretization process.

Next, the propagation of displacement in three directions and the corresponding normalized errors for three test points, ranging from -10 m to 10 m along the z-direction as shown in Figures 29–31, are explored, with the source point oscillating at the frequency of 2250 Hz. The test points, as shown in Figure 25, designated as $\overline{\mathrm{A}}_3$ $(-1.51, -2.50)$, $\overline{\mathrm{B}}_3$ (2.85, 0), and $\overline{\mathrm{C}}_3$ (2.26, 1.76), are located within the computational domain. Analysis of the figures reveals that the majority of normalized errors lie within the order of 10^{-4}, thereby reaffirming the high accuracy of this method. This reiterates the method's capability to accurately predict the response at the specified frequency for the tunnel structure affected by an external source point.

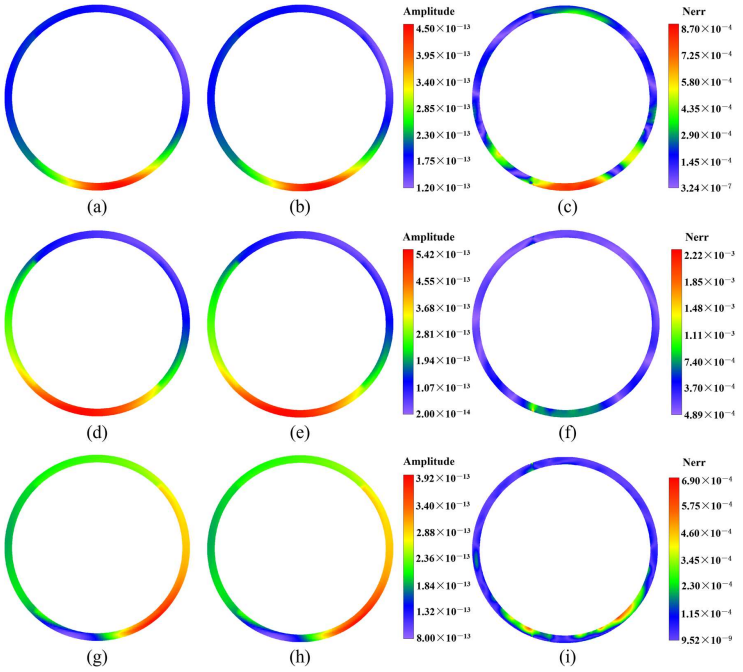


Figure 26. The contour plots of displacement fields at 2250 Hz on the plane $z = 3$ m for the first case of Example 3 computed by the 2.5D GFDM and the exact solutions, and the normalized errors between 2.5D GFDM and analytical solutions: (**a**,**d**,**g**) represent numerical solutions of amplitude of displacements u_x, u_y, and u_z, respectively; (**b**,**e**,**h**) represent exact solutions of amplitude of displacement u_x, u_y, and u_z, respectively; (**c**,**f**,**i**) represent the normalized errors between numerical solutions and exact solutions.

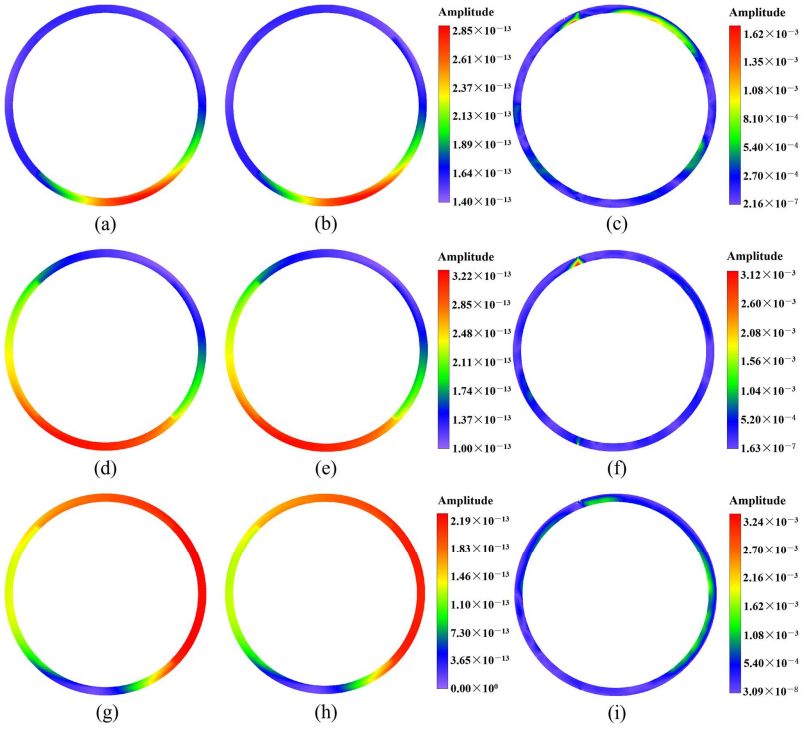


Figure 27. The contour plots of displacement fields at 3250 Hz on the plane $z = 5$ m for the first case of Example 3 computed by the 2.5D GFDM and the exact solutions, and the normalized errors between 2.5D GFDM and analytical solutions: (**a**,**d**,**g**) represent numerical solutions of amplitude of displacements u_x, u_y, and u_z, respectively; (**b**,**e**,**h**) represent exact solutions of amplitude of displacement u_x, u_y, and u_z, respectively; (**c**,**f**,**i**) represent the normalized errors between numerical solutions and exact solutions.

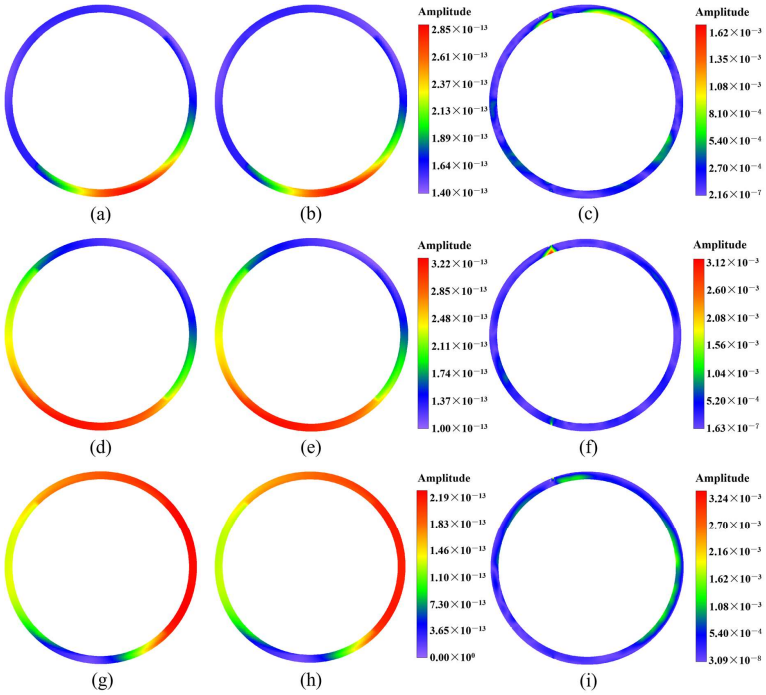


Figure 28. The contour plots of displacement fields at 4000 Hz on the plane $z = 1$ m for the first case of Example 3, computed by the 2.5D GFDM and the exact solutions, and the normalized errors between 2.5D GFDM and analytical solutions: (**a**,**d**,**g**) represent numerical solutions of amplitude of displacements u_x, u_y, and u_z, respectively; (**b**,**e**,**h**) represent exact solutions of amplitude of displacement u_x, u_y, and u_z, respectively; (**c**,**f**,**i**) represent the normalized errors between numerical solutions and exact solutions.

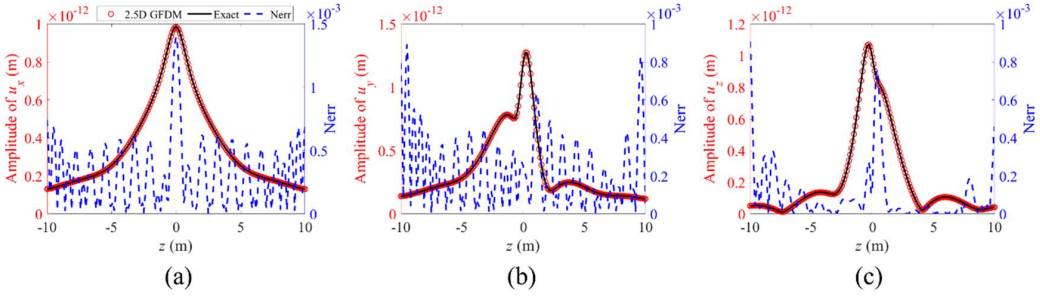


Figure 29. The propagation of amplitude of displacements (**a**) u_x, (**b**) u_y, and (**c**) u_z, and normalized errors between numerical solutions and exact solutions for point $\overline{\mathrm{A}}_3(-1.51, -2.50)$ from -10 m to 10 m along the z-axis at a frequency of 2250 Hz, in the first case of Example 3.

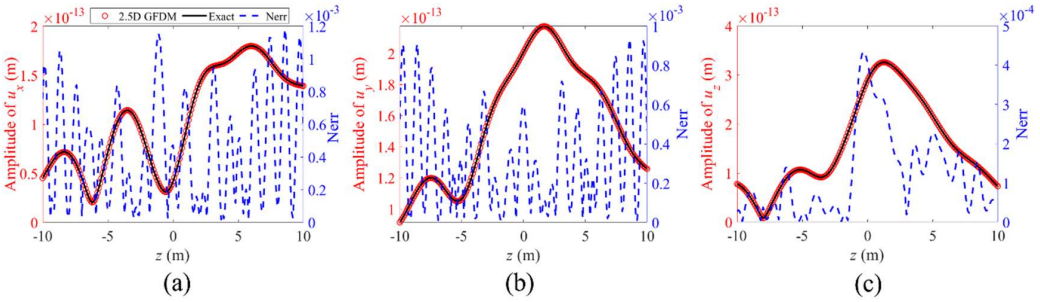


Figure 30. The propagation of amplitude of displacements (**a**) u_x, (**b**) u_y, and (**c**) u_z, and normalized errors between numerical solutions and exact solutions for point $\overline{\mathrm{B}}_3$ (2.85, 0) from -10 m to 10 m along the z-axis at a frequency of 2250 Hz, in the first case of Example 3.

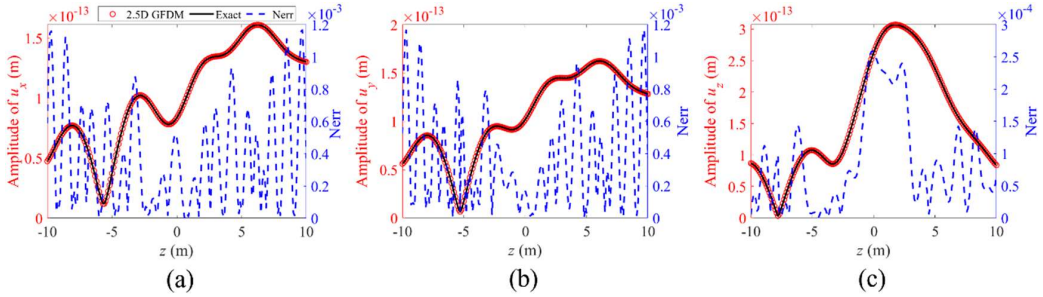


Figure 31. The propagation of amplitude of displacements (**a**) u_x, (**b**) u_y, and (**c**) u_z, and normalized errors between numerical solutions and exact solutions for point $\overline{C}_3$ (2.26, 1.76) from −10 m to 10 m along the z-axis at a frequency of 2250 Hz, in the first case of Example 3.

In Figures 32 and 33, the real and imaginary components of the displacements u_y and u_z as determined at the receiving points B_3 (2.85, 0, 1) and C_3 (2.26, 1.76, 1) over a frequency range of 500 to 4000 Hz using both the 2.5D GFDM and exact solutions are illustrated. Again, the figures demonstrate a strong correlation between the outcomes yielded by the proposed method and the analytical solutions at the specified frequencies. This reaffirms that the 2.5D GFDM demonstrates a significant level of accuracy in calculating the frequency response of tunnel-like structures with thinner walls when subjected to the influence of an external point source.

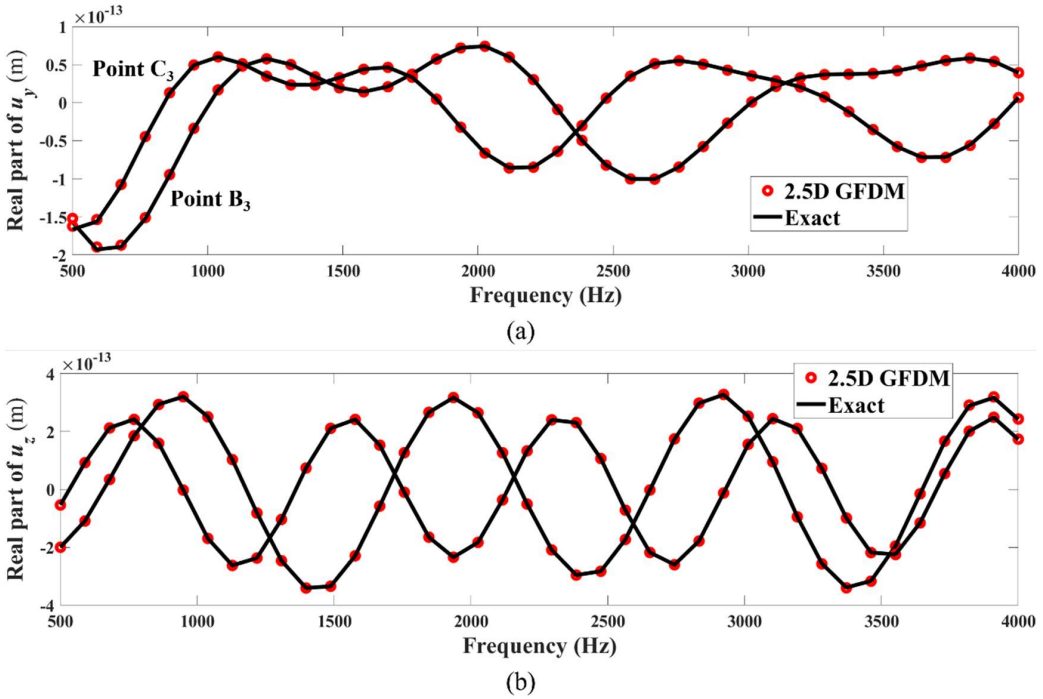


Figure 32. Real parts of frequency response of displacements (**a**) u_y and (**b**) u_z at test points B_3(2.85, 0, 1) and C_3 (2.26, 1.76, 1), in the first case of Example 3, computed by 2.5D GFDM and analytical solutions.

In the subsequent illustrative case, we delve into the performance of 2.5D GFDM within the context of computational engineering models. Specifically, we situate the source point within the confines of a tunnel structure, designated at the coordinates (0, −2, 0), to emulate a simplified representation of a vibration source attributable to an underground train, as shown in Figure 34. The remaining parameters for this case are aligned with the conditions outlined in the first case of Example 3.

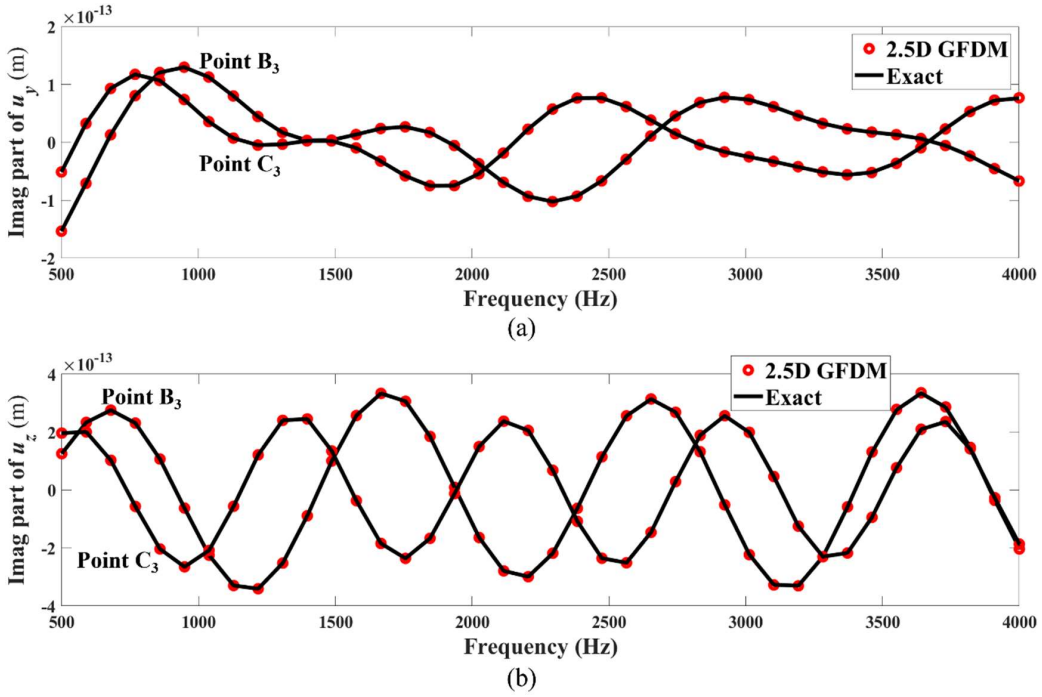


Figure 33. Imaginary parts of frequency response of displacements (**a**) u_y and (**b**) u_z at test points B_3 (2.85, 0, 1) and C_3 (2.26, 1.76, 1), in the first case of Example 3, computed by 2.5D GFDM and analytical solutions.

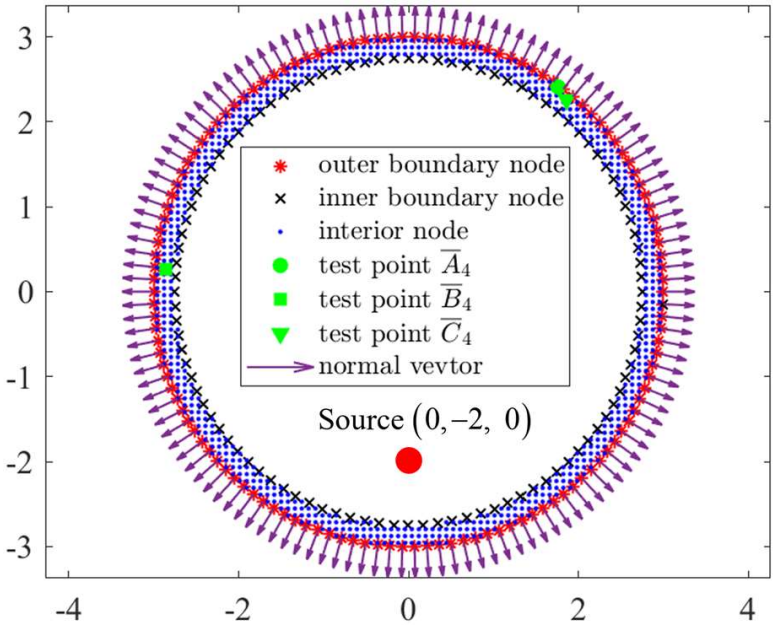


Figure 34. A schematic representation of uniform distribution of interior nodes and boundary nodes, along with an inner source point and test points for Example 3.

Figures 35–37 display the contour plots of the displacement amplitude on the xy plane at $z = 2$ m, which is influenced by a point source situated at coordinates $(0, -2, 0)$, for a frequency of 2250 Hz. Consistent with the first case of Example 3, the left section of the figures illustrates the computational results from the 2.5D GFDM. These results are contrasted with the central section, which portrays the displacement fields obtained from rigorous analytical solutions. The right section presents the contour plots of the normalized errors between the computational and analytical results. It is evident from the map of normalized errors that for the displacements in three dimensions, the error

distribution remains predominantly within the order of magnitude of 10^{-4} along most of the z-axis, indicating a substantial degree of concordance. Additionally, Figures 35 and 36 present contour plots analogous to those in Figure 33, but for different planes at $z = 5$ m and $z = 1$ m, with corresponding excitation frequencies of 3250 Hz and 4000 Hz, respectively. These figures, again, demonstrate a correlation between the numerical model's predictions and the accurate analytical results, echoing the findings from the earlier figures. Analogous to the first case in Example 3, the minor error oscillations in certain areas of the displacement fields across three directions, as shown in the figures, are caused by the distribution discrepancy between the computational interior nodes and boundary nodes. These fluctuations, including those mentioned in the previous examples, however, do not compromise the method's accuracy.

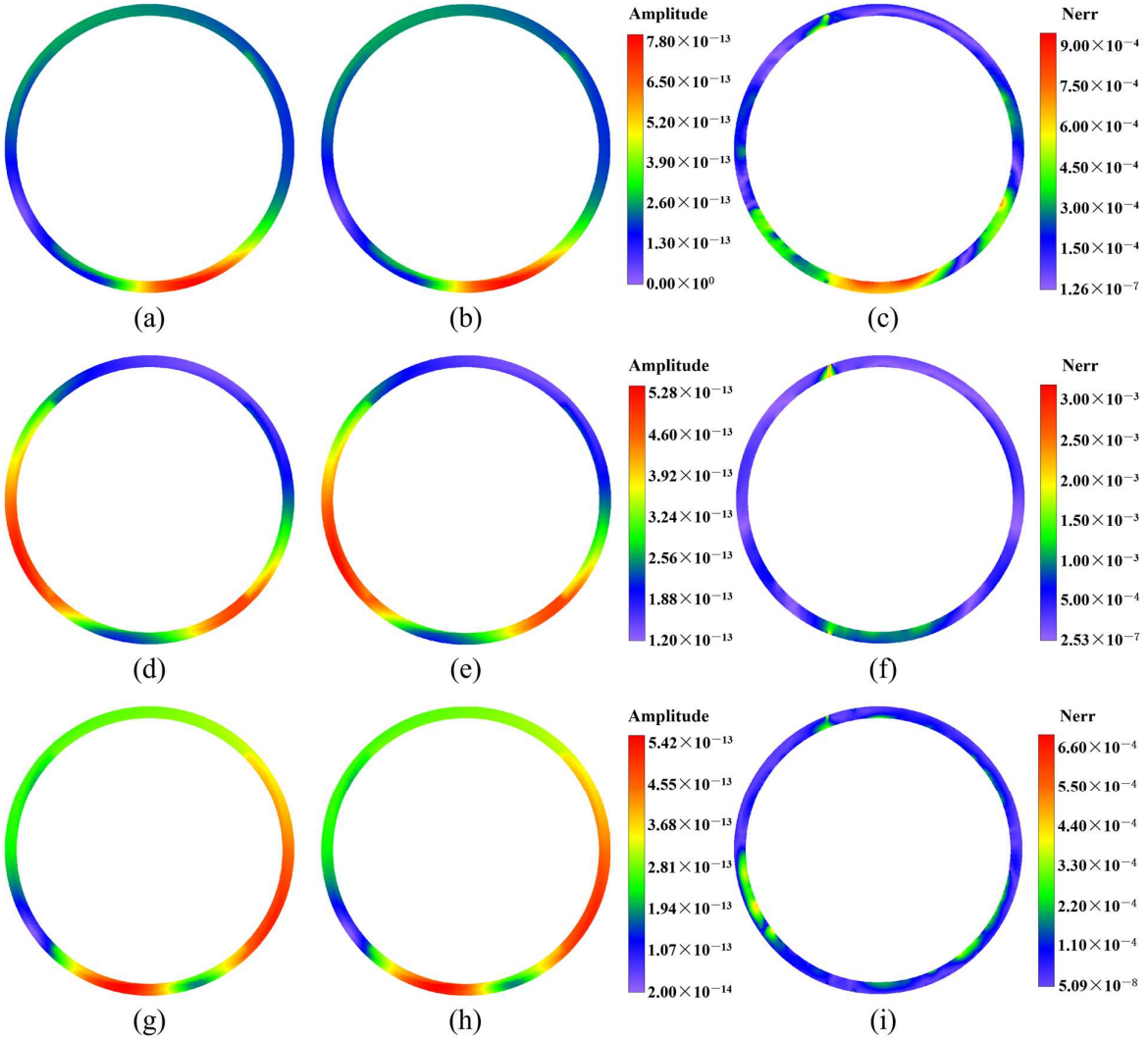


Figure 35. The contour plots of displacement fields at 2250 Hz on the plane $z = 2$ m for the second case of Example 1, computed by the 2.5D GFDM and the exact solutions, and the normalized errors between the proposed method and analytical solutions: (**a**,**d**,**g**) represent numerical solutions of amplitude of displacements u_x, u_y, and u_z, respectively; (**b**,**e**,**h**) represent exact solutions of amplitude of displacement u_x, u_y, and u_z, respectively; (**c**,**f**,**i**) represent the normalized errors between numerical solutions and exact solutions.

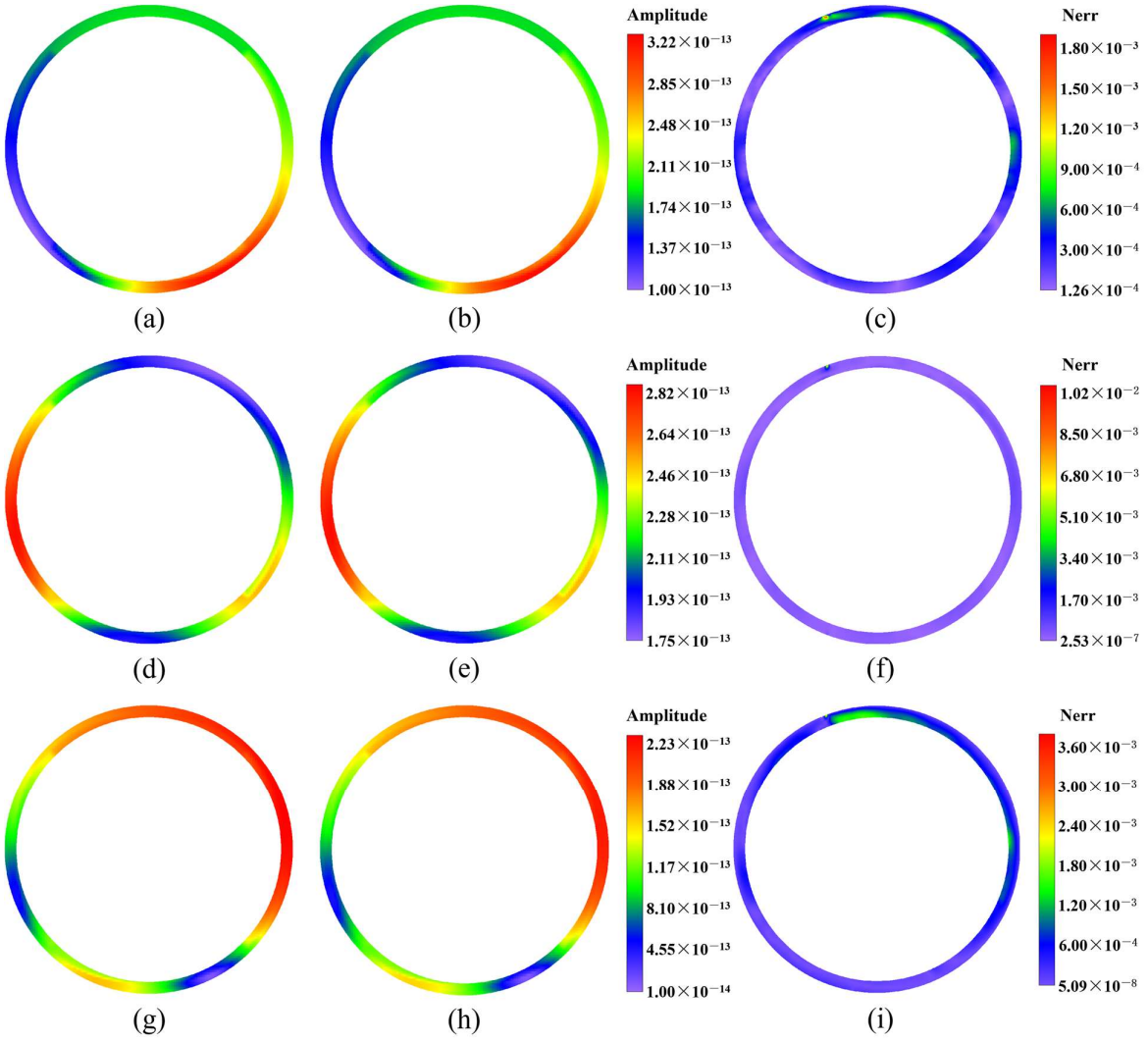


Figure 36. The contour plots of displacement fields at 2250 Hz on the plane $z = 5$ m for the second case of Example 1, computed by the 2.5D GFDM and the exact solutions, and the normalized errors between the proposed method and analytical solutions: (**a**,**d**,**g**) represent numerical solutions of amplitude of displacements u_x, u_y, and u_z, respectively; (**b**,**e**,**h**) represent exact solutions of amplitude of displacement u_x, u_y, and u_z, respectively; (**c**,**f**,**i**) represent the normalized errors between numerical solutions and exact solutions.

Subsequently, this investigation delves into the propagation of displacement and the corresponding normalized errors in three directions for three test points along the z-axis, ranging from -10 m to 10 m, with the source point oscillating at a frequency of 2250 Hz, as shown in Figures 38–40. The test points, designated as $\overline{\mathrm{A}}_4$ (1.76, 2.41), $\overline{\mathrm{B}}_4$ (-2.85, 0.27), and $\overline{\mathrm{C}}_4$ (1.86, 2.26), are positioned within the computational domain. A meticulous review of the graphical data reveals that the normalized errors generally lie within 10^{-4}, except for a few localized peaks, thereby confirming the high accuracy of this method in ascertaining the propagation of displacement in the z-direction. This further underscores the capability of 2.5D GFDM not only to accurately predict the response of the tunnel structure affected by an external point source at the specified frequency but also to demonstrate good accuracy in forecasting the vibrations of the tunnel structure caused by internal vibration sources.

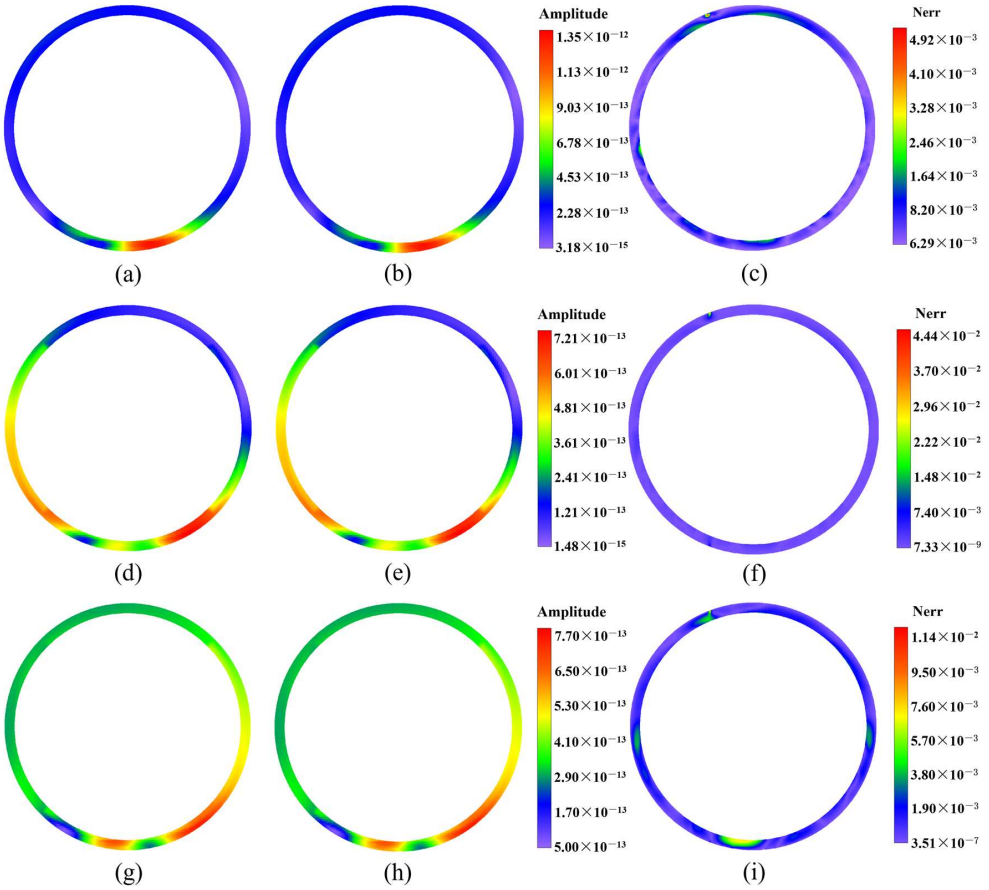


Figure 37. The contour plots of displacement fields at 4000 Hz on the plane $z = 1$ m for the second case of Example 1, computed by the 2.5D GFDM and the exact solutions, and the normalized errors between the proposed method and analytical solutions: (**a**,**d**,**g**) represent numerical solutions of amplitude of displacements u_x, u_y, and u_z, respectively; (**b**,**e**,**h**) represent exact solutions of amplitude of displacement u_x, u_y, and u_z, respectively; (**c**,**f**,**i**) represent the normalized errors between numerical solutions and exact solutions.

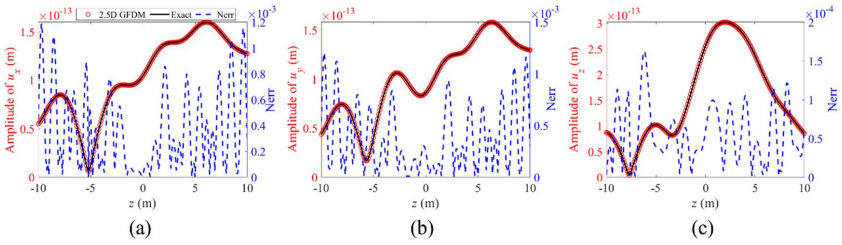


Figure 38. The propagation of amplitude of displacements (**a**) u_x, (**b**) u_y, and (**c**) u_z, and normalized errors between numerical solutions and exact solutions for point $\overline{\mathrm{A}}_4(1.76, 2.41)$ from -10 m to 10 m along the z-axis at a frequency of 2250 Hz, in the second case of Example 3.

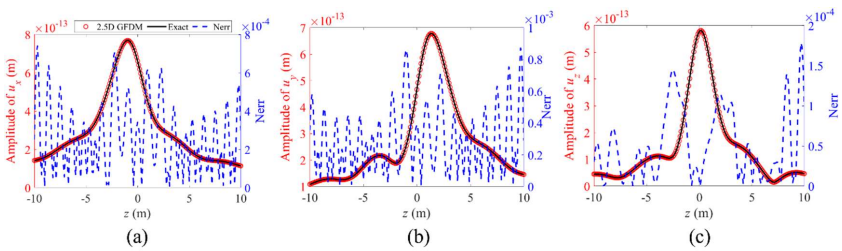


Figure 39. The propagation of amplitude of displacements (**a**) u_x, (**b**) u_y, and (**c**) u_z, and normalized errors between numerical solutions and exact solutions for point $\overline{\mathrm{B}}_4(-2.85, 0.27)$ from -10 m to 10 m along the z-axis at a frequency of 2250 Hz, in the second case of Example 3.

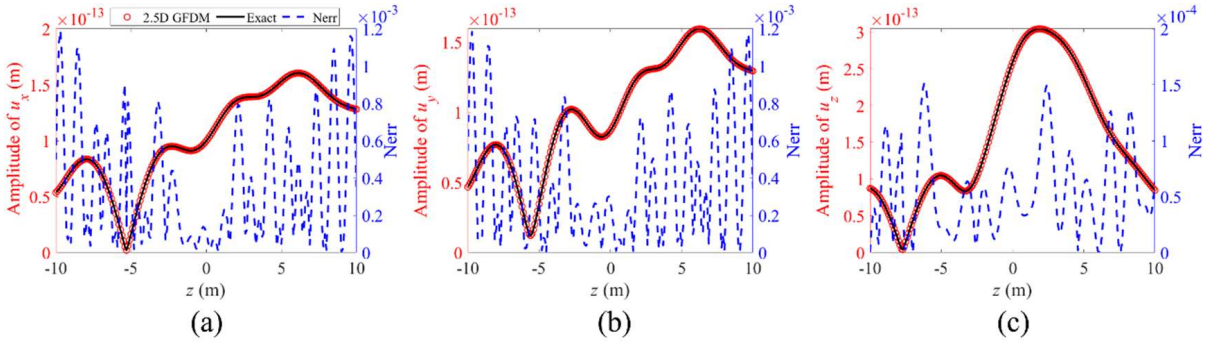


Figure 40. The propagation of amplitude of displacements (**a**) u_x, (**b**) u_y, and (**c**) u_z, and normalized errors between numerical solutions and exact solutions for point $\overline{C}_4$ (1.86, 2.26) from −10 m to 10 m along the z-axis at a frequency of 2250 Hz, in the second case of Example 3.

Figures 40–42 present the real and imaginary parts of displacement components at points $B_4(-2.85, 0.27, 1)$ and $C_4(1.86, 2.26, 1)$ over a frequency range of 500 to 4000 Hz, with results obtained through both the 2.5D GFDM and exact solutions. The strong agreement between the proposed method and the analytical solutions can be evidently observed, which confirms the reliability of the 2.5D GFDM. This highlights its capability to accurately predict the frequency response of the tunnel structure caused by internal vibration sources within the tunnel. In the second case of Example 3, the collective findings from the research affirm the efficacy of the method in question. This high level of consistency between 2.5D GFDM and exact solutions suggests that the 2.5D GFDM demonstrates potential in predicting the responses of tunnel structures to vibrations induced by underground railway trains.

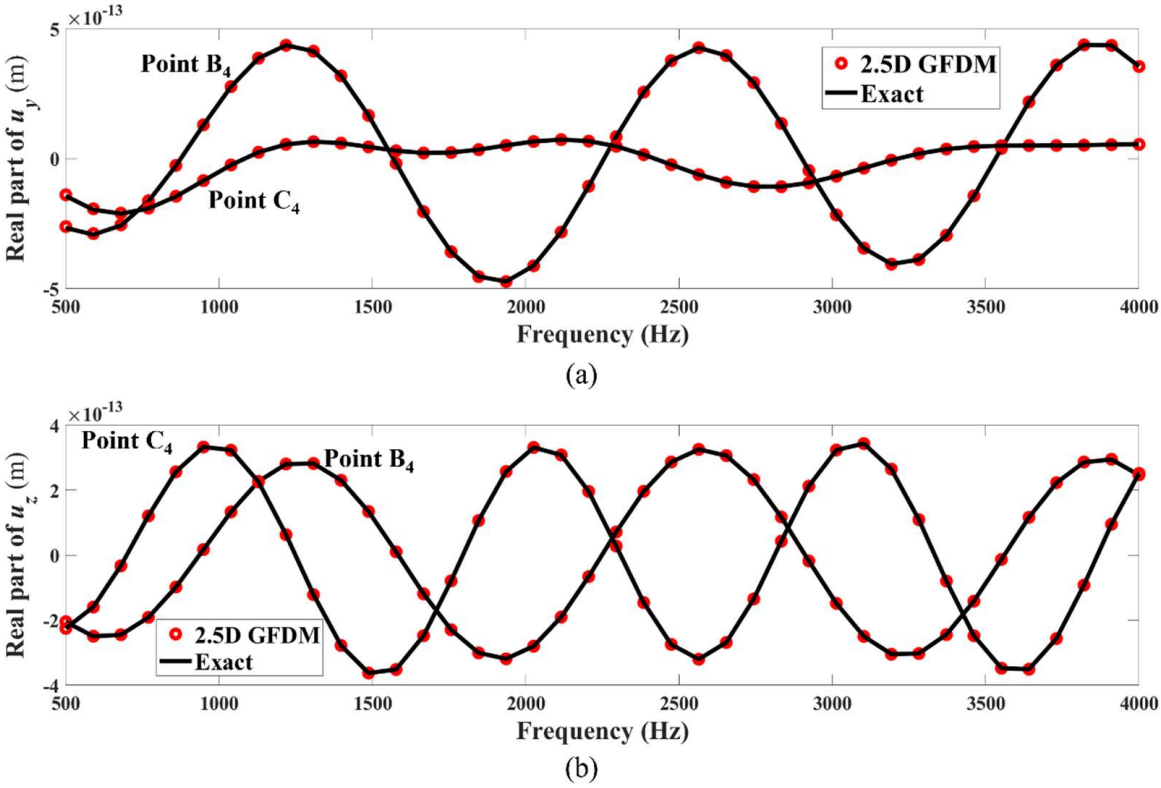


Figure 41. Real parts of frequency response of displacements (**a**) u_y and (**b**) u_z at test points $B_4(-2.85, 0.27, 1)$ and $C_4(1.86, 2.26, 1)$, in the second case of Example 3, computed by 2.5D GFDM and analytical solutions.

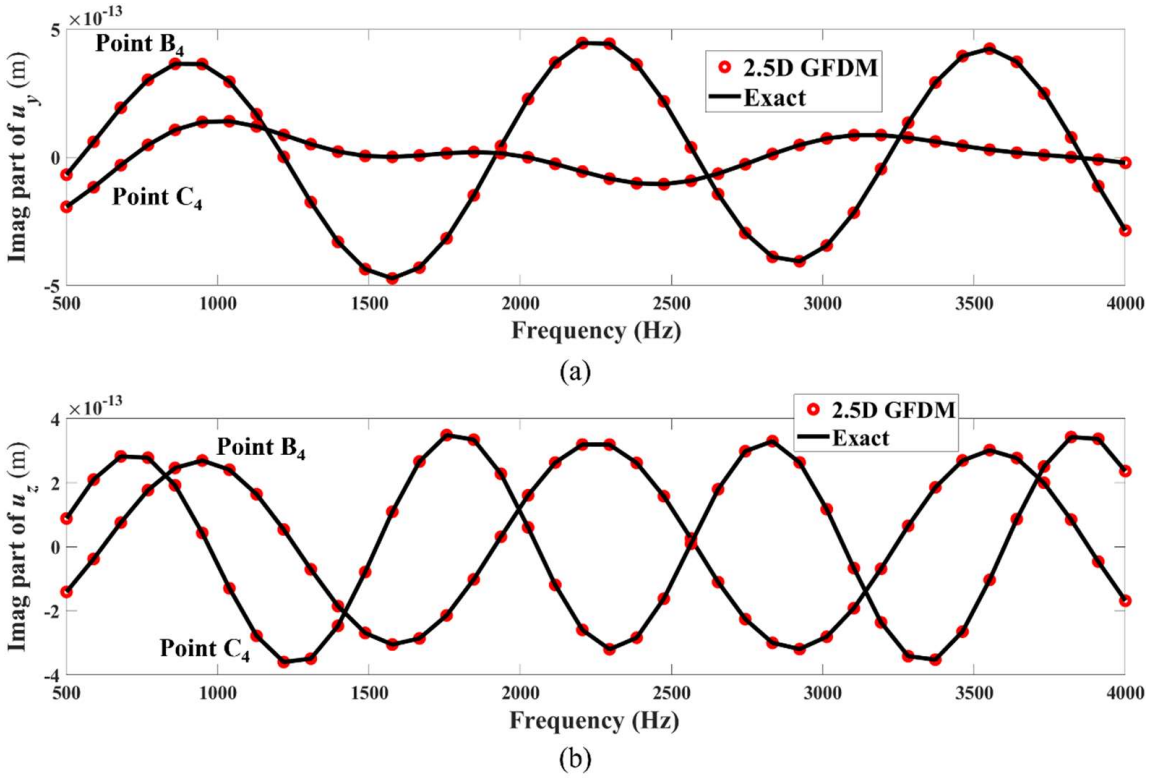


Figure 42. Imaginary parts of frequency response of displacements (**a**) u_y and (**b**) u_z at test points $B_4(-2.85, 0.27, 1)$ and $C_4(1.86, 2.26, 1)$, in the second case of Example 3, computed by 2.5D GFDM and analytical solutions.

5. Conclusions

This paper presents a method that combines 2.5D technology with the GFDM to solve the three-dimensional elastic wave propagation problem with an invariant cross-section in a certain direction. By employing the spatial Fourier transform, the complex three-dimensional problem is transformed into a more computationally convenient two-dimensional problem in the frequency-wavenumber domain. The resulting two-dimensional problem is then solved using the novel mesh-free numerical method GFDM, and the obtained solutions in the frequency-wave number domain are converted back into three-dimensional numerical solutions through the inverse Fourier transform. To investigate the performance of this method, three numerical examples were selected, and the numerical solutions of each example, including two cases in Example 3, were thoroughly compared with their corresponding exact solutions.

In Example 1, the two-dimensional numerical solutions in the frequency-wave number domain demonstrate the accuracy of the mesh-free numerical algorithm GFDM. Based on this, the three-dimensional numerical solutions obtained through the inverse Fourier transform, whether for the displacement field on the xy planes or the displacement response in the z-direction, show the considerable accuracy and stability of the 2.5D GFDM. Example 2 demonstrates that the 2.5D GFDM not only calculates the displacement field on xy planes and the displacement response in the z-direction but also demonstrates high precision in calculating the frequency response at each point. Example 3 indicates that the 2.5D GFDM can calculate engineering problems such as the impact of vibrations caused by subway trains on tunnel structures and also shows its excellent computational capability.

Given that this study primarily focuses on developing novel methodologies for addressing elastic wave propagation in axially infinite-extended structures, with a particular focus on underground engineering applications such as vibration wave propagation in

tunnels, further research is required to determine whether the 2.5D GFDM (Generalized Finite Difference Method) can be extended to handle cross-sections with higher geometric complexity (e.g., star-shaped or gear-shaped profiles). Key challenges needing in-depth investigation include (i) the strategic placement of calculation points in regions with highly complex geometries and (ii) potential hybrid/coupling approaches with other 2.5D numerical methods to enable simulations of more intricate geometries. The applicability of the 2.5D methodology is constrained by two principal factors: First, the approach inherently requires invariance in both cross-sectional configuration and material properties of the medium along the axial extension direction, thereby precluding its implementation in scenarios involving geometric or material heterogeneity in the longitudinal dimension. Second, stringent geometric scaling criteria must be satisfied, specifically that the model's longitudinal dimension should significantly exceed the characteristic wavelength to effectively mitigate boundary-induced elastic wave reflections, a critical prerequisite for maintaining numerical precision in semi-analytical simulation frameworks. Failing that, such issues necessitate the application of conventional 3D methodologies to achieve effective resolution.

In summary, the proposed 2.5D GFDM can solve the three-dimensional elastic wave propagation problem with an invariant cross-section, including practical engineering problems. More complex engineering problems, such as the impact of vibrations caused by subway rail transit on the ground, are still under study and will be presented in subsequent articles.

Author Contributions: Conceptualization, F.W.; Methodology, F.W., L.Q. and L.S.; Software, H.C.; Validation, X.Y.; Formal analysis, X.Y.; Writing—original draft, H.C.; Writing—review & editing, F.W. and L.S.; Visualization, L.Q.; Supervision, L.S. All authors have read and agreed to the published version of the manuscript.

Funding: The work described in this paper was supported by the National Natural Science Foundation of China (Nos. 12472203, 12402239, 12302263) and the Natural Science Foundation of Shandong Province of China (Grant Nos. ZR2023YQ005, ZR2024QA009, ZR2023QA013).

Data Availability Statement: The data that support the findings of this study are available from the corresponding author upon reasonable request.

Conflicts of Interest: The authors declare that they have no known competing financial interests or personal relationships that could have appeared to influence the work reported in this paper.

References

1. Bao, H.; Bielak, J.; Ghattas, O.; Kallivokas, L.F.; O'Hallaron, D.R.; Shewchuk, J.R.; Xu, J. Large-scale simulation of elastic wave propagation in heterogeneous media on parallel computers. *Comput. Methods Appl. Mech. Eng.* **1998**, *152*, 85–102. [CrossRef]
2. Ureña, F.; Benito, J.J.; Salete, E.; Gavete, L. A note on the application of the generalized finite difference method to seismic wave propagation in 2D. *J. Comput. Appl. Math.* **2012**, *236*, 3016–3025. [CrossRef]
3. Benito, J.; Ureña, F.; Salete, E.; Muelas, A.; Gavete, L.; Galindo, R. Wave propagation in soils problems using the Generalized Finite Difference Method. *Soil Dyn. Earthq. Eng.* **2015**, *79*, 190–198. [CrossRef]
4. Salete, E.; Benito, J.J.; Ureña, F.; Gavete, L.; Ureña, M.; García, A. Stability of perfectly matched layer regions in generalized finite difference method for wave problems. *J. Comput. Appl. Math.* **2017**, *312*, 231–239. [CrossRef]
5. Qu, W.; Gu, Y.; Fan, C.-M. A stable numerical framework for long-time dynamic crack analysis. *Int. J. Solids Struct.* **2024**, *293*, 112768. [CrossRef]
6. Moser, F.; Jacobs, L.J.; Qu, J. Modeling elastic wave propagation in waveguides with the finite element method. *Ndt E Int.* **1999**, *32*, 225–234. [CrossRef]
7. Serón, F.; Sanz, F.; Kindelan, M.; Badal, J. Finite-element method for elastic wave propagation. *Commun. Appl. Numer. Methods* **1990**, *6*, 359–368. [CrossRef]
8. Fu, Z.; Xi, Q.; Li, Y.; Huang, H.; Rabczuk, T. Hybrid FEM–SBM solver for structural vibration induced underwater acoustic radiation in shallow marine environment. *Comput. Methods Appl. Mech. Eng.* **2020**, *369*, 113236. [CrossRef]

9. Li, Y.; Dang, S.; Li, W.; Chai, Y. Free and forced vibration analysis of two-dimensional linear elastic solids using the finite element methods enriched by interpolation cover functions. *Mathematics* **2022**, *10*, 456. [CrossRef]
10. Jianfeng, Z. Quadrangle-grid velocity-stress finite-difference method for elastic-wave-propagation simulation. *Geophys. J. Int.* **1997**, *131*, 127–134. [CrossRef]
11. Zhang, W.; Zhang, Z.; Chen, X. Three-dimensional elastic wave numerical modelling in the presence of surface topography by a collocated-grid finite-difference method on curvilinear grids. *Geophys. J. Int.* **2012**, *190*, 358–378. [CrossRef]
12. Beskos, D.E. Boundary element methods in dynamic analysis. *Appl. Mech. Rev.* **1987**, *40*, 1–23. [CrossRef]
13. Liu, Y.; Rizzo, F. Hypersingular boundary integral equations for radiation and scattering of elastic waves in three dimensions. *Comput. Methods Appl. Mech. Eng.* **1993**, *107*, 131–144. [CrossRef]
14. Zou, M.-s.; Wu, Y.-s.; Liu, Y.-m.; Lin, C.-g. A three-dimensional hydroelasticity theory for ship structures in acoustic field of shallow sea. *J. Hydrodyn. Ser. B* **2013**, *25*, 929–937. [CrossRef]
15. Liu, Z.; Liu, L.; Liang, J.; Zhou, Y. An indirect boundary element method to model the 3-D scattering of elastic waves in a fluid-saturated poroelastic half-space. *Eng. Anal. Bound. Elem.* **2016**, *66*, 91–108. [CrossRef]
16. Perrey-Debain, E.; Trevelyan, J.; Bettess, P. Plane wave interpolation in direct collocation boundary element method for radiation and wave scattering: Numerical aspects and applications. *J. Sound Vib.* **2003**, *261*, 839–858. [CrossRef]
17. De Basabe, J.D.; Sen, M.K. A comparison of finite-difference and spectral-element methods for elastic wave propagation in media with a fluid-solid interface. *Geophys. J. Int.* **2015**, *200*, 278–298. [CrossRef]
18. Deckers, E.; Jonckheere, S.; Van Belle, L.; Claeys, C.; Desmet, W. Prediction of transmission, reflection and absorption coefficients of periodic structures using a hybrid wave based–finite element unit cell method. *J. Comput. Phys.* **2018**, *356*, 282–302. [CrossRef]
19. Moldovan, I.D.; de Freitas, J.A.T. Hybrid-Trefftz finite element models for bounded and unbounded elastodynamic problems. In *Proceedings of III European Conference on Computational Mechanics: Solids, Structures and Coupled Problems in Engineering: Book of Abstracts*; Springer: Dordrecht, The Netherlands, 2006; p. 400.
20. de Freitas, J.T. Hybrid finite element formulations for elastodynamic analysis in the frequency domain. *Int. J. Solids Struct.* **1999**, *36*, 1883–1923. [CrossRef]
21. Qin, Q.-H. Trefftz Finite Element Method and Its Applications. *Appl. Mech. Rev.* **2005**, *58*, 316–337. [CrossRef]
22. Fu, Z.-J.; Xi, Q.; Gu, Y.; Li, J.; Qu, W.; Sun, L.; Wei, X.; Wang, F.; Lin, J.; Li, W.; et al. Singular boundary method: A review and computer implementation aspects. *Eng. Anal. Bound. Elem.* **2023**, *147*, 231–266. [CrossRef]
23. Gu, Y.; Chen, W.; He, X.-Q. Singular boundary method for steady-state heat conduction in three dimensional general anisotropic media. *Int. J. Heat Mass Transf.* **2012**, *55*, 4837–4848. [CrossRef]
24. Liu, H.; Wang, F. A novel semi-analytical meshless method for the thickness optimization of porous material distributed on sound barriers. *Appl. Math. Lett.* **2024**, *147*, 108844. [CrossRef]
25. Wang, F.; Chen, W.; Tadeu, A.; Correia, C.G. Singular boundary method for transient convection–diffusion problems with time-dependent fundamental solution. *Int. J. Heat Mass Transf.* **2017**, *114*, 1126–1134. [CrossRef]
26. Liu, Q.; Šarler, B. Non-singular method of fundamental solutions for two-dimensional isotropic elasticity problems. *Comput. Model. Eng. Sci.* **2013**, *91*, 235–266.
27. Lan, L.; Zhou, Z.; Liu, H.; Wei, X.; Wang, F. An ACA-BM-SBM for 2D acoustic sensitivity analysis. *AIMS Math.* **2024**, *9*, 1939–1958. [CrossRef]
28. Fan, C.-M.; Chien, C.-S.; Chan, H.-F.; Chiu, C.-L. The local RBF collocation method for solving the double-diffusive natural convection in fluid-saturated porous media. *Int. J. Heat Mass Transf.* **2013**, *57*, 500–503. [CrossRef]
29. Fu, Z.-J.; Chen, W.; Yang, H.-T. Boundary particle method for Laplace transformed time fractional diffusion equations. *J. Comput. Phys.* **2013**, *235*, 52–66. [CrossRef]
30. Fan, C.; Liu, Y.; Chan, H.; Hsiao, S. Solutions of boundary detection problem for modified Helmholtz equation by Trefftz method. *Inverse Probl. Sci. Eng.* **2014**, *22*, 267–281. [CrossRef]
31. Liu, C.-S.; Kuo, C.-L.; Jhao, W.-S. The multiple-scale polynomial Trefftz method for solving inverse heat conduction problems. *Int. J. Heat Mass Transf.* **2016**, *95*, 936–943. [CrossRef]
32. Ju, B.; Gu, Y.; Wang, R. An enriched radial integration method for evaluating domain integrals in transient boundary element analysis. *Appl. Math. Lett.* **2024**, *153*, 109067. [CrossRef]
33. Wang, F.; Wang, C.; Chen, Z. Local knot method for 2D and 3D convection-diffusion-reaction equations in arbitrary domains. *Appl. Math. Lett.* **2020**, *105*, 106308. [CrossRef]
34. Qiu, X.; Yue, X. Solving time fractional partial differential equations with variable coefficients using a spatio-temporal meshless method. *AIMS Math* **2024**, *9*, 27150–27166. [CrossRef]
35. Chen, C.-S.; Fan, C.-M.; Wen, P. The method of approximate particular solutions for solving elliptic problems with variable coefficients. *Int. J. Comput. Methods* **2011**, *8*, 545–559. [CrossRef]
36. Chen, C.-S.; Fan, C.-M.; Wen, P. The method of approximate particular solutions for solving certain partial differential equations. *Numer. Methods Partial Differ. Equ.* **2012**, *28*, 506–522. [CrossRef]

37. Benito, J.; Urena, F.; Gavete, L. Influence of several factors in the generalized finite difference method. *Appl. Math. Model.* **2001**, *25*, 1039–1053. [CrossRef]
38. Gavete, L.; Gavete, M.; Benito, J. Improvements of generalized finite difference method and comparison with other meshless method. *Appl. Math. Model.* **2003**, *27*, 831–847. [CrossRef]
39. Prieto, F.U.; Muñoz, J.J.B.; Corvinos, L.G. Application of the generalized finite difference method to solve the advection–diffusion equation. *J. Comput. Appl. Math.* **2011**, *235*, 1849–1855. [CrossRef]
40. Chan, H.-F.; Fan, C.-M.; Kuo, C.-W. Generalized finite difference method for solving two-dimensional non-linear obstacle problems. *Eng. Anal. Bound. Elem.* **2013**, *37*, 1189–1196. [CrossRef]
41. Li, P.-W.; Fan, C.-M.; Chen, C.-Y.; Ku, C.-Y. Generalized finite difference method for numerical solutions of density-driven groundwater flows. *Comput. Model. Eng. Sci.* **2014**, *101*, 319–350.
42. Hosseini, S.M. Shock-induced two dimensional coupled non-Fickian diffusion–elasticity analysis using meshless generalized finite difference (GFD) method. *Eng. Anal. Bound. Elem.* **2015**, *61*, 232–240. [CrossRef]
43. Gavete, L.; Ureña, F.; Benito, J.J.; García, A.; Ureña, M.; Salete, E. Solving second order non-linear elliptic partial differential equations using generalized finite difference method. *J. Comput. Appl. Math.* **2017**, *318*, 378–387. [CrossRef]
44. Gu, Y.; Wang, L.; Chen, W.; Zhang, C.; He, X. Application of the meshless generalized finite difference method to inverse heat source problems. *Int. J. Heat Mass Transf.* **2017**, *108*, 721–729. [CrossRef]
45. Hua, Q.; Gu, Y.; Qu, W.; Chen, W.; Zhang, C. A meshless generalized finite difference method for inverse Cauchy problems associated with three-dimensional inhomogeneous Helmholtz-type equations. *Eng. Anal. Bound. Elem.* **2017**, *82*, 162–171. [CrossRef]
46. Sun, W.; Qu, W.; Gu, Y.; Zhao, S. Three-dimensional elastodynamic analysis employing the generalized finite difference method with arbitrary-order accuracy. *Comput. Math. Appl.* **2024**, *174*, 151–166. [CrossRef]
47. Zhang, F.; Li, P.-W.; Gu, Y.; Fan, C.-M. A space-time generalized finite difference scheme for long wave propagation based on high-order Korteweg-de Vries type equations. *Math. Comput. Simul.* **2025**, *228*, 298–312. [CrossRef]
48. Orkisz, J. Meshless finite difference method I. Basic approach. In Proceedings of the IACM-Fourth World Congress in Computational Mechanics, Buenos Aires, Argentina, 29 June–2 July 1998.
49. Li, P.-W.; Chen, W.; Fu, Z.-J.; Fan, C.-M. Generalized finite difference method for solving the double-diffusive natural convection in fluid-saturated porous media. *Eng. Anal. Bound. Elem.* **2018**, *95*, 175–186. [CrossRef]
50. Song, L.; Li, P.-W.; Gu, Y.; Fan, C.-M. Generalized finite difference method for solving stationary 2D and 3D Stokes equations with a mixed boundary condition. *Comput. Math. Appl.* **2020**, *80*, 1726–1743. [CrossRef]
51. Suchde, P.; Kuhnert, J. A meshfree generalized finite difference method for surface PDEs. *Comput. Math. Appl.* **2019**, *78*, 2789–2805. [CrossRef]
52. Ureña, F.; Salete, E.; Benito, J.J.; Gavete, L. Solving third-and fourth-order partial differential equations using GFDM: Application to solve problems of plates. *Int. J. Comput. Math.* **2012**, *89*, 366–376. [CrossRef]
53. Gu, Y.; Qu, W.; Chen, W.; Song, L.; Zhang, C. The generalized finite difference method for long-time dynamic modeling of three-dimensional coupled thermoelasticity problems. *J. Comput. Phys.* **2019**, *384*, 42–59. [CrossRef]
54. Ma, L.; Zhang, C.; Ouyang, H.; Yan, Q.; Yu, W. 2.5 D modelling of wave propagation in longitudinally curved viscoelastic structure using a coupled FEM-PML approach. *Eng. Struct.* **2021**, *226*, 111337. [CrossRef]
55. Sun, L.; Wei, X.; Chen, B. A meshless singular boundary method for elastic wave propagation in 2D partially saturated poroelastic media. *Eng. Anal. Bound. Elem.* **2020**, *113*, 82–98. [CrossRef]
56. Wei, X.; Liu, D.; Luo, W.; Chen, S.; Sun, L. A half-space singular boundary method for predicting ground-borne vibrations. *Appl. Math. Model.* **2022**, *111*, 630–643. [CrossRef]
57. Gu, Y.; Chen, W.; Fu, Z.-J.; Zhang, B. The singular boundary method: Mathematical background and application in orthotropic elastic problems. *Eng. Anal. Bound. Elem.* **2014**, *44*, 152–160. [CrossRef]
58. Liravi, H.; Arcos, R.; Clot, A.; Conto, K.F.; Romeu, J. A 2.5 D coupled FEM–SBM methodology for soil–structure dynamic interaction problems. *Eng. Struct.* **2022**, *250*, 113371. [CrossRef]
59. Liravi, H.; Clot, A.; Arcos, R.; Fakhraei, J.; Godinho, L.; Conto, K.F.; Romeu, J. A 2.5 D hybrid SBM-MFS methodology for elastic wave propagation problems. *J. Sound Vib.* **2024**, *586*, 118501. [CrossRef]
60. Sun, L.; Fu, Z.; Chen, Z. A localized collocation solver based on fundamental solutions for 3D time harmonic elastic wave propagation analysis. *Appl. Math. Comput.* **2023**, *439*, 127600. [CrossRef]
61. Aubry, D.; Clouteau, D.; Bonnet, G. Modelling of wave propagation due to fixed or mobile dynamic sources. In Proceedings of the Workshop Wave '94, Wave Propagation and Reduction of Vibrations, Ruhr-Universität Bochum, Germany, 8 December 1994; pp. 109–121.
62. Sheng, X.; Jones, C.; Petyt, M. Ground vibration generated by a harmonic load acting on a railway track. *J. Sound Vib.* **1999**, *225*, 3–28. [CrossRef]

63. Sheng, X.-Z.; Jones, C.; Petyt, M. Ground vibration generated by a load moving along a railway track. *J. Sound Vib.* **1999**, *228*, 129–156. [CrossRef]
64. Zeng, S.; Chen, F.; Li, D.; Chen, J.; Chen, J. A novel 2.5 D finite difference scheme for simulations of resistivity logging in anisotropic media. *J. Appl. Geophys.* **2018**, *150*, 144–152. [CrossRef]
65. Suchde, P. Particle-based adaptive coupling of 3D and 2D fluid flow models. *Comput. Methods Appl. Mech. Eng.* **2024**, *429*, 117199. [CrossRef]
66. Yang, S.-b.; Zhou, B.; Bai, C.-y. A generalized 2.5-D time-domain seismic wave equation to accommodate various elastic media and boundary conditions. *Pure Appl. Geophys.* **2021**, *178*, 2999–3025. [CrossRef]
67. Amado-Mendes, P.; Costa, P.A.; Godinho, L.M.; Lopes, P. 2.5 D MFS–FEM model for the prediction of vibrations due to underground railway traffic. *Eng. Struct.* **2015**, *104*, 141–154. [CrossRef]
68. Tadeu, A.J.; Kausel, E. Green's functions for two-and-a-half-dimensional elastodynamic problems. *J. Eng. Mech.* **2000**, *126*, 1093–1097. [CrossRef]
69. Xing, Y.; Song, L.; He, X.; Qiu, C. A generalized finite difference method for solving elliptic interface problems. *Math. Comput. Simul.* **2020**, *178*, 109–124. [CrossRef]
70. Lin, J.; Chen, W.; Sun, L. Simulation of elastic wave propagation in layered materials by the method of fundamental solutions. *Eng. Anal. Bound. Elem.* **2015**, *57*, 88–95. [CrossRef]

Disclaimer/Publisher's Note: The statements, opinions and data contained in all publications are solely those of the individual author(s) and contributor(s) and not of MDPI and/or the editor(s). MDPI and/or the editor(s) disclaim responsibility for any injury to people or property resulting from any ideas, methods, instructions or products referred to in the content.